Early Neoproterozoic Tectonics in the Godhra–Chhota Udepur Sector: Evidence for Two-Stage Accretion in the Great Indian Proterozoic Fold Belt

Anwesa Banerjee, Nicole Sequeira, Nathan Cogné, N. Prabhakar, Abhijit Bhattacharya

GeoScienceWorld
Lithosphere
Volume 2022, Article ID 9322892, 29 pages
https://doi.org/10.2113/2022/9322892

Lithosphere

Research Article

Early Neoproterozoic Tectonics in the Godhra–Chhota Udepur Sector: Evidence for Two-Stage Accretion in the Great Indian Proterozoic Fold Belt

Anwesa Banerjee,[1] **Nicole Sequeira**,[2] **Nathan Cogné**,[3] **N. Prabhakar**,[4] **and Abhijit Bhattacharya**[1]

[1]*Department of Geology and Geophysics, Indian Institute of Technology, Kharagpur 721 302, India*
[2]*School of Earth, Ocean and Atmospheric Sciences, Goa University, Taleigao Plateau, Goa 403 206, India*
[3]*Univ Rennes, CNRS, Geosciences Rennes, UMR 6118, 35000 Rennes, France*
[4]*Department of Earth Sciences, Indian Institute of Technology Bombay, Powai, Mumbai 400 076, India*

Correspondence should be addressed to Anwesa Banerjee; anwesabanerjee91@gmail.com
and Abhijit Bhattacharya; abbhat55@gmail.com

Received 27 July 2021; Accepted 9 March 2022; Published 8 April 2022

Academic Editor: Songjian Ao

The Great Indian Proterozoic Fold Belt (GIPFOB) is a curviplanar highly-tectonized zone of Precambrian crystalline rocks. In the GIPFOB, the N/NNE-striking western arm (the Aravalli Delhi Fold Belt, ADFB) and the E-striking southern arm consisting of the Chottanagpur Gneiss Complex (CGC) and the central/southern domains of the Satpura Mobile Belt (SMB) converge at the Godhra-Chhota Udepur sector. To investigate the tectonics of the sector, we combine the results of analyses of mesoscale and regional structures, U-Pb (zircon) geochronology, and monazite chemical dating to constrain the convergence. The sector is dominated by an ensemble of shallow-dipping granitoid mylonites (D2 deformation) and recumbently folded anatectic granulite-facies basement gneisses interleaved with allochthonous greenschist/epidote-amphibolite facies supracrustal rocks thrust top-to-the-south. The shallow-dipping carapace is traversed by a network of E-striking steep-dipping shear zones with sinistral and N-down kinematics (D3 deformation). The D3 shear zone hosted granitoids exhibit E-striking suprasolidus deformation fabrics and chessboard microstructures. In the shallow-dipping carapace, the partly overlapping stretching lineations associated with D2-D3 deformations share low-angle obliquities with the W/WNW plunging hinges of D2 recumbent folds and the upright/moderately-inclined D3 folds in the basement gneisses and the supracrustal rocks. The transition from thrust-dominated (D2) to wrench-dominated (D3) deformation involved flipping of Y and Z strain axes for similar orientations of orogen-parallel stretching caused by N-S shortening. U-Pb LA-ICP-MS (zircon) and monazite chemical dates suggest the D2-D3 deformation and felsic plutonism occurred at 0.95–0.90 Ga, the pre-D2 high-grade metamorphism in the anatectic gneisses at 1.7–1.6 Ga. The 0.95–0.90 Ga structures in the Godhra-Chhota Udepur are identical to those in CGC-SMB in the southern arm and terminate the N/NNE-striking structures in the ADFB. We suggest the GIPFOB comprises two Early Neoproterozoic accretion zones, e.g., the western arm (ADFB) and the younger (GC-SMB-CGC) southern arm.

1. Introduction

Map-scale curvature of orogens, fold-and-thrust belts, and shear zones can be a primary feature, i.e., primary arcs [1] formed due to progressive deformation [1–4] or an outcome of secondary processes that curve an initially linear crustal segment [1, 5–8]. Primary arc curvature is controlled by the characteristics of the predeformational sedimentary basin involved in thrusting during collision, such as the strength of the rocks and the depth and slope of the detachment [1, 5, 9]. Progressive arcs are possibly the most common type of map-scale curvatures [1–4] that form at collision zones and progressively develop their curvature during the same orogenic cycle ([2], and references therein).

Progressive arcs are commonly "indenter-controlled" [1–4], but other mechanisms may prevail. On the other hand, secondary curvatures develop by buckling that accommodates rotation around a vertical axis [1] in subsequent deformation cycles unrelated to the formation of the originally linear belt [2].

The Great Indian Proterozoic Fold Belt, GIPFOB (Figures 1(a) and 1(b); [10, 11]) is a crustal-scale highly-tectonized zone that extends E-W in central India and appears to curve into the NNE-striking Aravalli Delhi Fold Belt (ADFB) in western India. The southern arm of the GIPFOB comprises the domains of the Chottanagpur Gneiss Complex (CGC) and the Satpura Mobile Belt (SMB); both domains exhibit E-striking tectonic fabrics. The NNE-striking ADFB constitutes the western arm of the GIPFOB (Figure 1). The GIPFOB possibly extends eastward into the Garo-Goalpara sector (Figure 1(a)) in the Shillong-Meghalaya Gneiss Complex [12]. The southern arm is deemed to be the zone of accretion between the North India Block (NIB) and the South India Block (SIB); the western arm is sandwiched between the NIB and the Marwar Craton (MC) [10]. The boundaries of the crustal domains vis-à-vis the orogen are for most parts uncertain. The GIPFOB has been correlated with the Capricorn Orogen [13] within the Columbia supercontinent [14, 15], and the Albany Fraser Orogen [16] in the Rodinia Supercontinent [17]. The E-striking southern arm is also known as the Central Indian Tectonic Zone (CITZ) [18].

The origin of the curvature in the GIPFOB in west-central India where the two arms converge (Figure 1) is yet to be investigated. A compilation of trends of dominant tectonic fabrics in the ADFB accretion orogen (data source: https://bhukosh.gsi.gov.in) indicates that at its southern tip the NNE-striking structures are reoriented E-W in the neighboring Godhra-Chhota Udepur sector (Figure 2). In this study, we examine the implications of this reorientation or "bend" of tectonic trends in ADFB based on an analysis of mesoscale structures and deformation kinematics in the Godhra-Chhota Udepur sector (Figure 2). Zircon U-Pb dating and monazite chemical ages in critical samples from the sector are used to constrain the ages of magmatic, metamorphic, and deformation events. This study is the first attempt to integrate the new structural-geochronological data with existing information in the Godhra-Chhota Udepur sector into a coherent analysis of the regional scale tectonics for explaining the "bend" in the GIPFOB. The results of this study are aimed at understanding the nature and significance of the purported bend, prior to correlating the GIPFOB with contemporaneous crustal-scale accretion zones across drifted continental fragments.

2. Geological Background of the Godhra-Chhota Udepur Sector

The Godhra-Chhota Udepur sector was chosen for the study for three reasons. The sector is located at the inner arc of a possible oroclinal bend (Figure 1(b)) and at the zone where the two arms (ADFB and the CITZ) of the GIPFOB converge (Figure 2). Also, the available geological information in the sector is fragmentary at best. The Precambrian crystalline rocks in the Godhra-Chhota Udepur (GC) sector are grouped into four lithodemic units: (a) a suite of variably deformed (massive, foliated, and mylonitic) grey and pink colored blastoporphyritic granitoids, collectively termed as the Godhra granite; (b) mesoscale outcrops of (not shown in Figures 3(a) and 3(b)) multiply – deformed biotite ± hornblende bearing anatectic quartzofeldspathic gneiss intruded by the granite body; (c) the Champaner Group which consists of greenschist/epidote-amphibolite facies mica schist and calc-schists, quartzites and micaceous quartzite, metadolomites, Mn-rich horizons, meta-arenites, deformed intraformational conglomerates, amphibolites, and ultramafic rocks; and (d) the Lunavada group consisting of quartzite, phyllite, schist, and minor carbonates metamorphosed at greenschist facies conditions [20]. In the Champaner Group, the abundances of meta-carbonate and Mn-rich horizons decrease, and mafic-ultramafic rocks increase from south to north. The lithodemic units in the southern part are partly obscured by the Upper Cretaceous Deccan volcanics and the infratrappean Lameta Formation and intertrappean Bagh beds (Figure 3; nomenclature after Sahni et al. [21]).

The Godhra granite is neither a mineralogically homogenous unit nor a distinct structural entity (details in Section 3). The emplacement ages of the different parts of the Godhra granite are Late Mesoproterozoic to Early Neoproterozoic, e.g., 955 ± 20 Ma, Rb–Sr method [22], 1168 ± 30 Ma, Rb-Sr method [23], 1050 ± 50 Ma, Sm–Nd method [24], 965 ± 40 Ma, Rb–Sr method [25], and 950 Ma, Rb–Sr method [26]. The 955 Ma age [22] is the most cited age for the emplacement of the Godhra granite [27–30].

The banded anatectic gneisses that occur as enclaves with the expansive Godhra granitoids are the structurally the oldest lithodemic unit [27–29] in the Godhra-Chhota Udepur sector, but no age determinations exist for the rocks. The gneisses are composed of multiply deformed alternate layers of biotite ± hornblende rich domains and quartzofeldspathic leucosomes and minor amphibolite bands [28]. By contrast, the granitoids are massive to foliated, and apophytic within the gneisses; the granitoids lack the multiple folds in the gneiss enclaves. The gneisses exhibit three deformation events, D1-D3 [28]. The D2 deformation is manifested by tight to isoclinal folds formed by refolding of the S1 axial planes (corresponding to the D1 deformation). The axial planes (S2) of the D2 folds strike NW/WNW. The asymmetric D3 folds on S2 produced WNW-striking steep-dipping S3 axial planes; these D3 folds are considered to be broadly coeval with the emplacement of Godhra granite [28].

The structural evolution of the Champaner Group of metasedimentary rocks of low metamorphic grade is controversial [28–32]. The rocks unconformably overlie the gneisses [33] and have experienced multiple deformation events [28, 30–32, 34–36]. The earliest deformation led to recumbent folding; these folds were overprinted by open to tight, gentle to moderately plunging folds with WNW-ESE to E-W striking axial traces. Locally developed N-S striking folds and shear zones mark the last phase of deformation in the rocks [35]. The emplacement of the Godhra granite

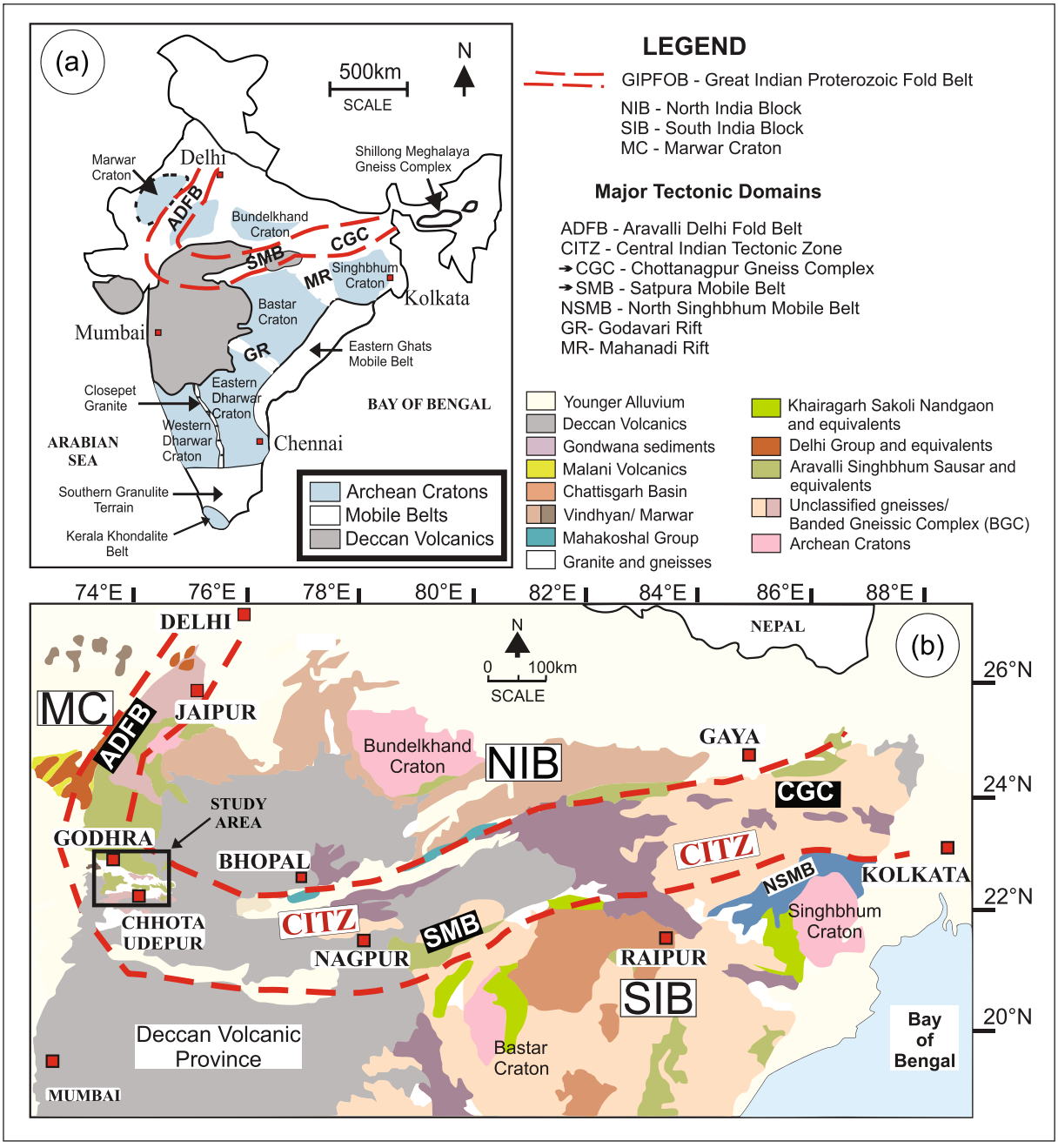

FIGURE 1: Generalized geological map of the Great Indian Proterozoic Fold Belt, GIPFOB (shown with broken red lines), and its location within India. The different crustal domains that make up the GIPFOB and the Godhra-Chhota Udepur sector are located in both maps. NIB, SIB, and MC are acronyms for the North India Block, the South India Block, and the Marwar Craton, respectively. SMB and CGC are acronyms for the Satpura Mobile Belt and the Chottanagpur Gneiss Complex. The E-striking arm of the GIPFOB vis-à-vis the CGC-SMB composite together constitutes the Central Indian Tectonic Zone (CITZ), but the southern and the northern margins of the CITZ, and their longitudinal extensions, are poorly constrained [19].

is syn-to post-tectonic with respect to the Champaner Group of rocks [35, 36]. The initial phase of granite intrusion was broadly syn-tectonic with the earliest deformation in the Champaner Group, whereas the later granitoids led to thermal metamorphism of the Champaner rocks [36].

The Lunavada Group of rocks comprises quartzite, phyllite, schist, and minor carbonates, metamorphosed at greenschist facies conditions [20]. Three deformation events (D1-D3) accompanied by regional metamorphism are recorded in the rocks [28, 37, 38]. The D1-D2 deformations are coaxial and produced NE-trending folds [28]. In the southern part of the belt, the WNW-ESE to E-W trending D3 folds are prominently developed; the superposition of D3 over the D1-D2 folds produced type I interference

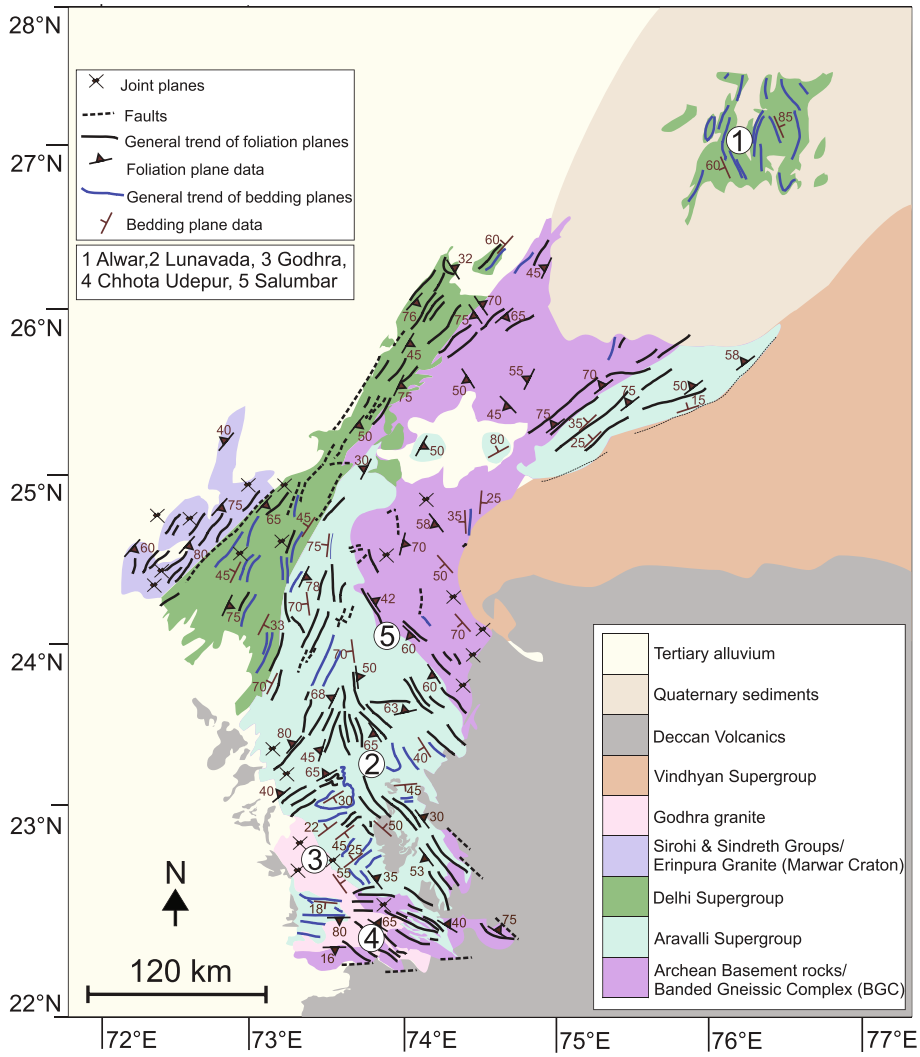

FIGURE 2: Generalized tectonic trends in the NNE-striking Aravalli-Delhi Fold Belt (ADFB). Note the ADFB structures are reoriented near the Godhra-Chhota Udepur sector at the southern tip of the ADFB.

patterns [28, 38]. M_1 metamorphism is synchronous with D1 deformation; the $M_{2\text{-}1}$ metamorphism was syn-D2, and the retrograde $M_{2\text{-}2}$ metamorphism occurred during the waning phase of D2 and the early phase D3; granite emplacements are post D3 in the Lunavada rocks [37, 38].

3. Field Relations and Mesoscale Structures: This Study

The Godhra-Chhota Udepur sector was structurally mapped (Figure 3) based on observations at 395 field stations. The relevant stereoplots of planar and linear deformation fabrics in the anatectic gneisses, the foliated granitoids, and the supracrustal rocks are shown in Figure 4. This study does not address the structures within the Lunavada Group nor the boundary relations between the basement gneisses and granitoids in the Godhra-Chhota Udepur sector (Figure 3). The major findings in this study (Figure 3) are the following: (a) two shallow-dipping (dip < 35°) domains comprising gently-dipping granite mylonites (S and S > L tectonite) and older gneisses exhibiting recumbent to gently-inclined folds on gneissic layering; (b) the supracrustal rocks in several domains/klippen tectonically overlying the basement of the gneiss and granitoids are erosional remnants of an allochthonous unit thrust top-to-the-south; (c) the shallow-dipping tectonic fabrics (dip < 35°, adopted by us) in the basement and the cover rocks are steepened in the limbs due to folding superposition in and adjacent to the networks of W/WNW-striking steep-dipping left-lateral transpressional shear zones. Therefore, the areal extent of the shallow-dipping domains shown in Figure 3 is a lower estimate. This is because the restriction in the dip amount precludes accommodating locations in which the shallow-dipping tectonic fabrics become steeper than 35° due to the folding associated with the younger W/WNW-striking shear zones.

3.1. Basement Gneisses. The basement gneisses are mineralogically diverse. The gneisses are dominated by mesocratic varieties in which biotite ± hornblende rich layers alternate with quartz, K-feldspar, and plagioclase bearing leucocratic

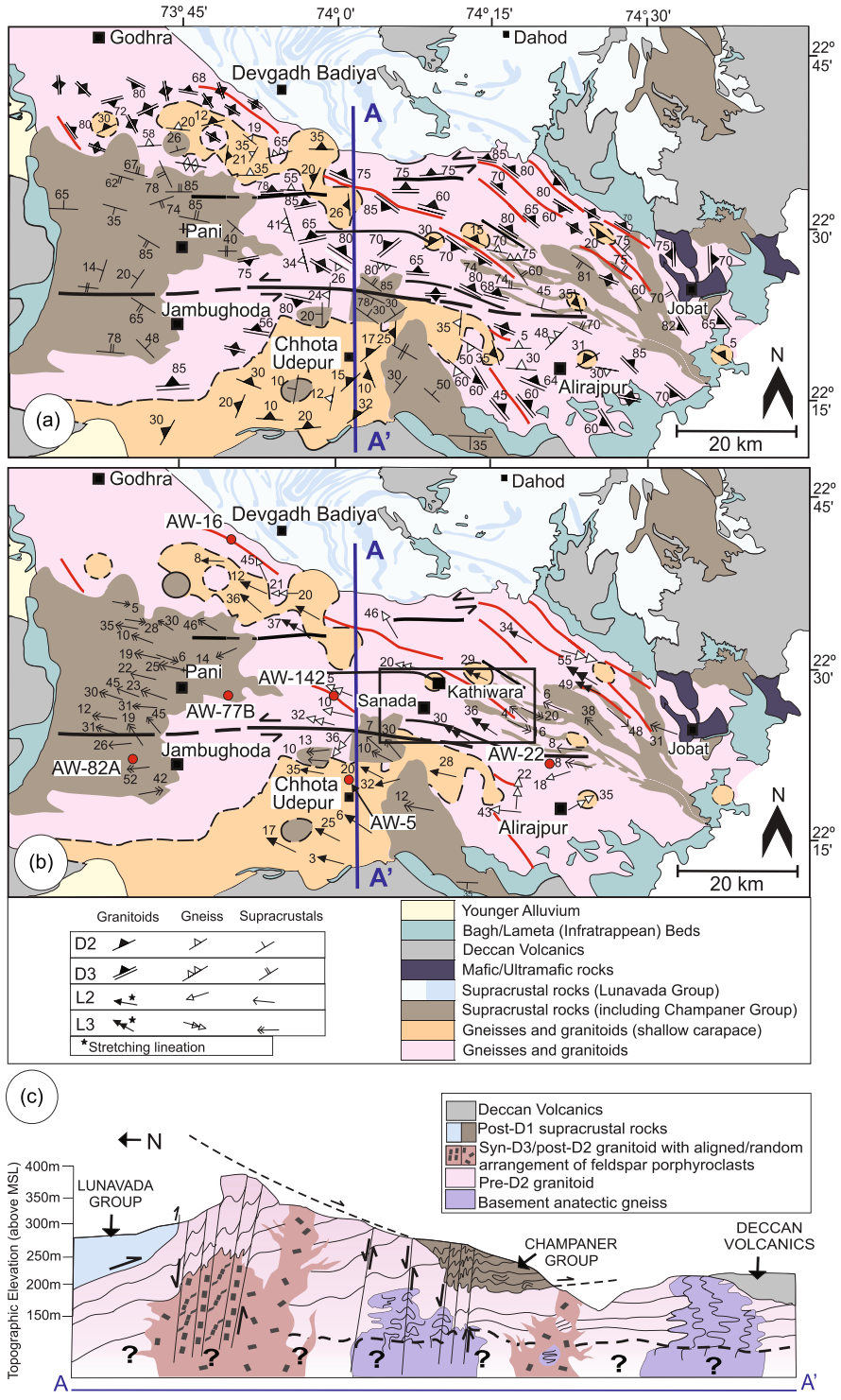

FIGURE 3: Structural map of the Godhra-Chhota Udepur sector showing (a) planar structures and (b) linear structures identified in this study. The lithological map of the Godhra-Chhota Udepur sector is simplified after the District Resource maps of Jabua, Panchmahal, and Vadodara of the Geological Survey of India. Axial plane foliation (S2) and fold axis and stretching lineations (L2) are associated with D2 deformation; same scheme is adopted for S3, L3, and D3 (legend in (b)). The box in (b) corresponds to Figure 7(a). The locations of the zircon and monazite dated samples (red circles) are shown in (b). Note within the Godhra granite, the anatectic gneisses occur as mesoscale enclaves, but regional-scale exposures of the gneisses, the oldest lithodemic unit in the area, are lacking. In the scale of the map, therefore, these gneisses do not appear in (a, b). (c) A schematic geologic section along A-A′ exhibits the structural relations among the lithodemic units (see text for discussion). The lower broken line (conjectural) is taken to suggest the décollement below which the basement rocks may be unaffected by thrusting. Note the section was drawn to illustrate the different structural units of the Godhra granite, but these units were not comprehensively mapped throughout the area. Therefore, the colors of lithodemic units in (a, b) and (c) do not match.

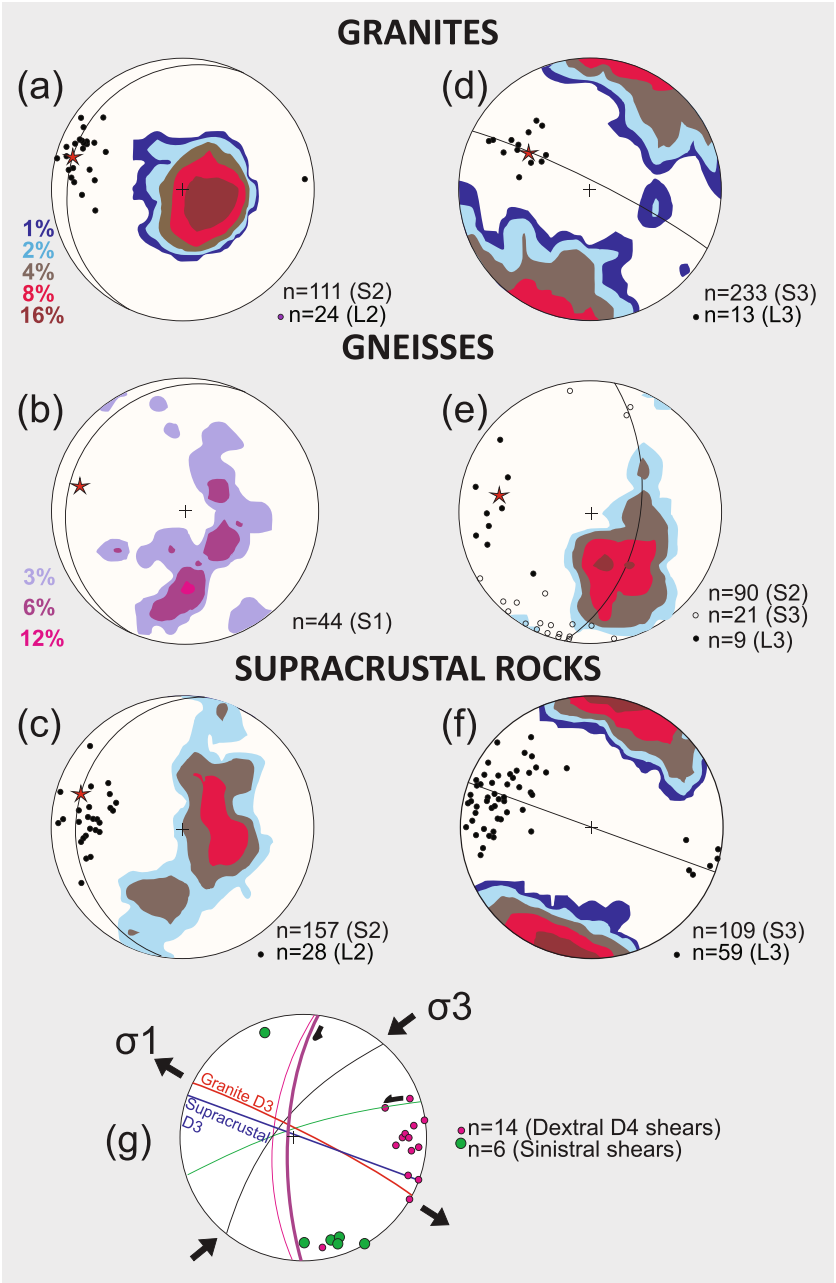

FIGURE 4: Lower hemisphere stereoplots of planar and linear structural elements in foliated granites (a, d), basement gneisses (b-e), and the supracrustal rocks (c, f). Summary of D4 planar structures in gneiss, granitoid, and supracrustal rocks (g). (a) Contours of poles S2 planar fabrics in foliated granites in the tectonic mélange; black dots are D2 stretching lineations (L2). The great circle girdle corresponds to the mean orientation of the S2 foliation in the granites. (b) Contoured poles of recumbent to gently-inclined D2 folds on pre-S2 foliation in gneisses. Star represents the pole to the best-fit girdle (not shown) on the pre-S2 poles. The great circle is the mean orientation of the foliated granites in the tectonic mélange (adopted from "a"). (c) Contoured poles to pre-S2 foliation in supracrustal rocks. Star is the best-fit β-axis to the contoured poles. Black dots are D2 fold axes obtained from pre-S2/S2 intersection lineations. (d) Contours of poles to steep-dipping S3 foliations in granite; black dots are L3 stretching lineations. (e) Poles to S2 foliations in gneisses (contoured), D3 fold axes in black dots, and poles to S3 foliation (in open circles). Star represents the β-axis (D3 fold axis) to the contoured best-fit S2 girdle. (f) Contoured poles to S2 foliations in supracrustal rocks. Black dots are D3 fold axes obtained from S2/S3 intersection lineations and D3 crenulations. (g) Mean orientations of N-striking and ENE-striking shear zones. The E-striking great circles correspond to the mean orientation of D3 foliation in steep-dipping granites, and the mean axial plane of D3 supracrustal rocks. The stress axes are indicated.

layers. Melanocratic gneisses, which occur in subordinate amounts, consist of quartz – plagioclase ± K – feldspar leucocratic layers (+ garnet) in the biotite-dominated melanocratic matrix (rare garnet, cordierite, and sillimanite). These gneisses are interleaved with minor proportions of nonanatectic amphibolites and plagioclase-scapolite-clinopyroxene-quartz bearing meta-carbonate gneisses. Muscovite is lacking except as a rare retrograde mineral associated with chlorite. In spite of the lithological variations, the structural evolution in the gneisses is fairly uniform. The earliest fabric (S1; D1 deformation) is defined by centimeters to subdecimeter wide leucosome layers interlayered with melanocratic layers dominated by biotite and/or hornblende (Figure 5(a)). D1 folds are rarely preserved [28]. D2 folds are tight to isoclinal and recumbent to gently-inclined in geometry in the shallow-dipping domains. The D2 axial planes (S2) are poorly marked in the round-hinged biotite-poor gneisses (Figure 5(b)), but are penetrative and characterized by a well-defined schistosity in the biotite-rich gneisses (Figure 5(c)). The vergence of D2 folds indicates a top-to-the-south transport (Figure 5(c)). In rare outcrops of biotite gneisses, limited amounts of syn-D2 melt occur along the axial planes of D2 folds (Figure 5(c)); but syn-D2 leucosomes are lacking in the biotite-poor quartzofeldspathic gneisses.

The D3 folds are W/WNW–trending upright to steeply-inclined with subhorizontal to gently-plunging hinge lines (Figure 5(d)). The interlimb angles of these folds vary widely. In the shallow-dipping low-D3 strain domains, the D3 folds are barely discernible in outcrop scale, but the folds become progressively tighter as the W/WNW-striking steep-dipping D3 shear zones are approached. Within the W-striking D3 mylonite zones, the D1-D2 composite fabrics (S1-S2) are eventually transposed subparallel to the D3 mylonite fabric (S3) and occur obliquely to the mylonite fabric as rafts in low-D3 strain domains (Figure 5(e)).

The D3 fabrics (S3) are modified by locally-developed steep-dipping D4 shears; in rare outcrops, the shears occur in pairs. The strike of the shears with apparent dextral kinematics varies between 10° and 30°N (mean 20°N), and the other set of sinistral (apparent) shears trend between 45 and 70°N (mean~60°N). The ENE-striking sinistral shears are rare, but the NNE-trending dextral shears are prominent in some outcrops, and in rare instances, extend up to few kilometers. These sets of shears occur together in two outcrops, but their contemporaneity could not be unambiguously assessed.

3.2. Granitoids. Granitoids in the Godhra-Chhota Udepur sector comprise several varieties in decreasing areal abundance, e.g., (type-A) grey-colored, medium-grained, broadly equigranular (with rare cm-sized circular feldspar phenocrysts) hornblende-biotite granites, generally massive to weakly foliated, and modally rich (>10 vol%) in ferromagnesian phases (Figure 6(a)); (type-B) coarse-grained, highly inequigranular pink-colored granite-granodiorite with high modal amounts of euhedral to subhedral K-feldspar megacrysts measuring up to 6 cm in length (augen-shaped in deformed varieties) and contain profuse (>10 vol%) biotite aggregates (Figures 6(b) and 6(c)); and (type-C) coarse-grained, white-colored granodiorite having an equigranular sugary appearance, and a low abundance (<5 vol%) of ferromagnesian minerals, biotite > hornblende (Figure 6(d)). In the granite-granodiorites, dynamically recrystallized quartz, K-feldspar, and plagioclase are the major minerals with biotite, hornblende, sphene, apatite, and ilmenite [39]; randomly-oriented retrograde chlorite and epidote replacing hornblende/biotite occur as minor phases. Monazite and zircon are accessory phases.

The anatectic gneisses occur as mesoscopic to macroscopic enclaves within the granitoids (Figures 6(a) and 6(d)); the granitoids are intrusive into the gneisses. With respect to the tectonic fabrics in the gneisses, the granitoids can be grouped as those predating the D2 deformation (both grey- and pink-colored granitoids), and the pink- and white-colored granitoids emplaced post-D2 to syn-D3. In zones of high-D2 strain, the pre-D2 granitoids are shallow-dipping S and S-L tectonites (Figure 6(e)). The gentle NW-plunging stretching lineations in these granitoids are defined by the alignment of biotite/hornblende, quartz ribbons, and aggregates of recrystallized feldspar grains. The post-D2, pre-D3 granitoids are structurally and texturally complex; one such granitoid pluton is discussed below. In syn-D3 pink granitoids (Figure 6(c)), euhedral phenocrysts of K-feldspar occur as trains of end-to-end touching grains and grain imbrications typical of magmatic flow [40].

A granitoid pluton in and around Sanada (~20 km NE of Chhota Udepur) was structurally mapped (Figure 7(a)). The E-W elongate pluton consists of a bulged centre (~10 km wide) and two E-W striking asymmetric tails that extend ~35 km (Figure 7(a)). The steep-dipping D3 foliation in the bordering high-grade gneisses wraps around the pluton. The tails of the pluton coincide with two steep-dipping E-striking D3 sinistral shear zones (Figure 7(a)). The core of the central bulge comprises two textural types: (a) massive granitoids (no mesoscale fabrics; Figure 7(b)) composed of randomly-oriented large (up to 5 cm long) euhedral K-feldspar (microcline) megacrysts (subhedral K-feldspar phenocrysts occur in subordinate amounts) and (b) foliated granitoids (Figure 7(c)) composed of weakly-aligned trains of euhedral to subhedral microcline phenocrysts embedded in a finer-grained mosaic of recrystallized quartz-feldspar grains couple-of-mm in size, and biotite aggregates. Quartz and biotite are interstitial to the framework of microcline crystals in the massive varieties; but in the foliated varieties, quartz ribbons and shape-preferred aggregates of biotite wrap around the microcline clasts. The mantle of the pluton exhibits a well-developed tectonic foliation defined by biotite and quartz lentils in a finer-grained mosaic of recrystallized minerals; K-feldspars are mostly augen-shaped and define well-developed S-C fabrics (Figure 7(d)). These features extend from the mantle into the asymmetric tails of the pluton. In the intensely-sheared pluton margin around the central bulge, and in the tails, the former K-feldspar phenocrysts occur as augen (Figure 7(e)). Asymmetric clasts and rare S-C-C' fabrics in the granitoid tectonites attest to persistent sinistral kinematics; stretching lineations are rare even in the most intensely sheared varieties. The meso- to

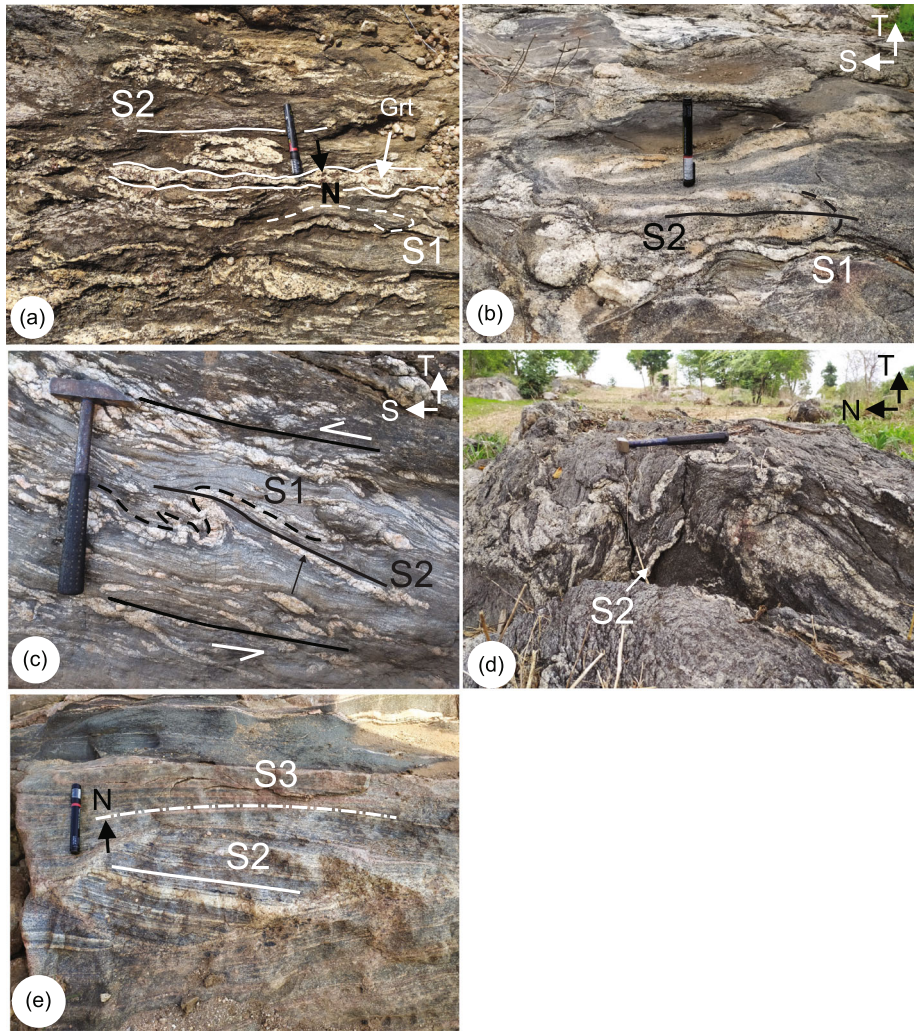

FIGURE 5: Field photographs of mesoscale structures (details in text) in basement gneisses. (a) Plan view (horizontal surface) of a biotite-rich anatectic gneiss showing D2 isoclinal folds and boudins on melt layers intrafolial to a penetrative S2 schistosity. Note (i) the biotite flakes folded at the fold hinges, and (ii) the occurrence of garnet (arrow). (b, c) Section views (vertical surface) of D2 recumbent folds in (b) biotite-poor gneiss and (c) biotite-rich gneiss (S2 is the axial plane of D2 folds on pre-S2 metatexite layers). Note (i) the shallow-dipping D2 foliation in the gneiss, (ii) top-to-the south movement on D2 foliation, and (iii) pinch-and-swell structures (arrow) in leucosome parallel to S2 axial planes in anatectic biotite-gneiss. (d) Profile section of D3 gently-plunging upright fold on S2 foliation in biotite-rich anatectic gneiss (hammerhead points North). (e) Plan view of D2 fabrics in rafts of gneisses in D3 mylonite zones. Locations of photographs are in Supplementary Material 1.

microstructural and kinematic features are consistent with a post-D2 emplacement of the pluton that subsequently experienced D3 deformation. The D3 deformation intensely affected the pluton margin, but the core of the pluton largely retained its magmatic texture. In several post-D2 deformed pink-colored granitoid outcrops, chess-board subgrain structures indicative of deformation at high-T, >650°C in quartz [41] is common (Figure 8(a)). In the granitoids, aggregates of K-feldspar hosted within microcracks oriented orthogonal to the long axis of quartz lentils (Figure 8(b)) indicate submagmatic flow aided by microcracking in the cooling pluton (cf. [42]). These meso- and microscale magmatic features, lacking in the pre-D2 granitoids, indicate that the D3 deformation affected the post-D2 plutons closely following their emplacement.

Locally, the D3 fabrics in the granitoids are sinuous neighboring D4 shears (Figure 6(f)). Commonly, these shears host melts, and the curving of the D3 fabrics near the D4 shears continued as long as the melt existed; beyond the melt-bearing zones, the shears peter out and the D3 fabrics are not warped [43]. This suggests the nucleation of the D4 shears occurred in the presence of melt through a feedback relationship [43, 44]. Due to the melt-hosted nature of the conjugate NNE and ENE-striking shears, we consider the nucleation of the shears to be broadly contemporaneous with, albeit closely following, the D3 deformation at supra-solidus conditions in the granitoids.

3.3. Supracrustal Rocks. The Champaner Group of rocks occurring in four isolated domains is composed of sheared

FIGURE 6: Field photographs showing mesoscale structures in granitoids. (a) Grey-granitoid with biotite-rich enclave. Note the penetrative foliation (arrow) in the enclave; the foliation is absent in the granitoid. (b) Pink granitoid showing steep-dipping S-C fabrics defined by K-feldspar augen. (c) Pink-colored granitoid showing the trains and tiles of euhedral phenocrysts of K-feldspar. (d) Steeply-dipping white-colored foliated granitoid with an enclave of biotite-rich gneiss. (e) Shallow-dipping granitoid mylonites. (f) Networks of sinistral N-trending ductile melt-filled shears off-setting warped D3 deformation fabric in granitoid. Locations of photographs are in Supplementary Material 1.

intraformational meta-conglomerates (with pebble/cobble-sized round/subrounded quartz clasts) and mica schists (white mica – chlorite – clinozoisite/epidote ± biotite ± garnet ± kyanite), quartzites and micaceous quartzites, meta-carbonates (calcite-dolomite-tremolite-antigorite-quartz), Mn-rich horizons, meta-arenites (quartz – K – feldspar – plagioclase – muscovite > biotite), amphibolites (amphibole-plagioclase-clinozoisite/epidote-quartz), and ultramafic rocks (tremolite – antigorite ± anthophyllite – titanite ± quartz). The southern domains are dominated by meta-carbonate, mica schist/micaceous quartzite, meta-arenite, meta-conglomerate, and Mn-rich horizons [36]. Meta-carbonate horizons are uncommon in the northern domain dominated by amphibolites, mica schists, and micaceous quartzites and ultramafic rocks. The contact between the basement gneisses/granitoids and supracrustal rocks is exposed in several localities. In zones of low-D3 strain, the contact between the flat-lying to gently-dipping tectonic fabrics in the overlying supracrustal rocks and the basement is intensely deformed or mylonitized. No persistent basal conglomerate layer was observed to demarcate the contact, but in a few outcrops sheared oligomict conglomerate adjacent to the mylonitized basement showed upward size reduction in the quartz clasts.

The supracrustal rocks exhibit three sets of tectonic fabrics. In D3 low-strain domains, the earliest fabric (S0) is a color banding (sedimentary layering) best observed in meta-dolomites and quartzites (Figure 9(a)). These layers exhibit isoclinal folds (D1 deformation) with the development of a shallow-dipping axial planar metamorphic fabric, S1. The D1 folds are round hinged in quartzites and meta-arenites (Figure 9(b)), sharp hinged in meta-carbonates

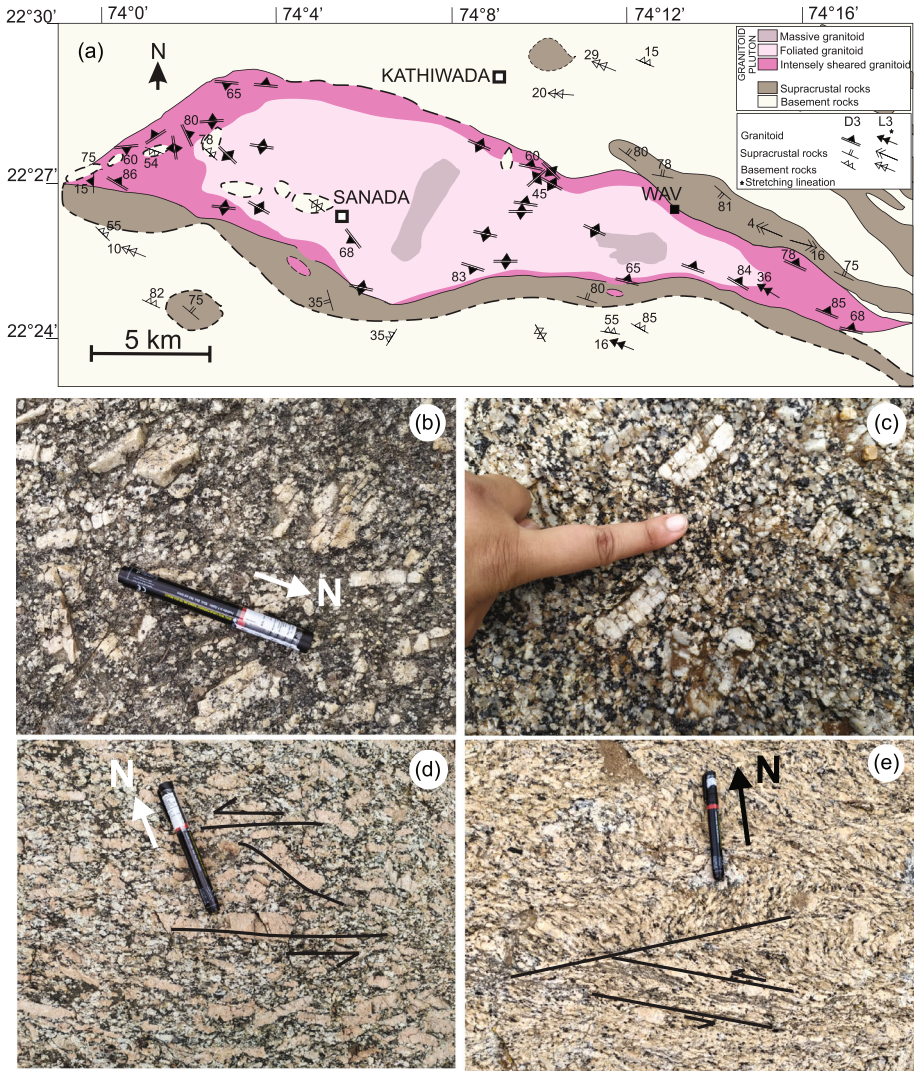

FIGURE 7: (a) Structural-lithological map of the core-mantled structured Sanada granitoid pluton with asymmetric tails. (b–d) Plan view images of mesoscale structures in the granitoid; pen-head points north. (b) Randomly-oriented euhedral K-feldspar porphyries in the core of the pluton; note the mesoscale tectonic fabrics are lacking, and the absence of recrystallization in K-feldspar phenocrysts. (c) Trains of euhedral to subhedral phenocrysts of K-feldspar in a finer-grained recrystallized mineral matrix close to the northern margin of the pluton. Finger is shown for scale only. (d) Augen of K-feldspar phenocrysts showing S-C fabrics in sheared granitoids in the eastern tail of the pluton. (e) K-feldspar augen showing sinistral kinematics and ENE-striking extensional shear bands in granitoid in the eastern tail of the pluton. Locations of photographs are in Supplementary Material 1.

(Figure 9(a)), but rarely preserved or obliterated in mica/calc schists. The S1 fabric is either recumbently folded or transposed (D2 deformation) parallel to a flat-lying to gently-dipping S2 axial plane schistosity (Figure 9(c)). In contrast to the gneisses, the D1 and D2 fabrics in the mica schists, metacarbonates, and amphibolites (and interleaved ultramafic rocks in the north) in the supracrustal unit are defined by minerals of lower metamorphic grade, e.g., quartz – chlorite – muscovite ± clinozoisite/epidote ± biotite in mica schist, talc-tremolite-antigorite in a recrystallized mosaic of calcite-dolomite-quartz in metacarbonates, cummingtonite – hornblende quartz in amphibolite, and tremolite – antigorite ± anthophyllite in ultramafic rocks.

In profile sections of open W/E-plunging D2 folds and normal to the D2 stretching lineations (L2) in granites, the D2 folds in the supracrustal rocks display top-to-the south kinematics (Figure 9(d)). In and neighboring D3 shear zones, the D1-D2 axial plane fabrics are thrown into a set of upright to steeply-inclined folds with subhorizontal to gently-plunging hinge lines (Figure 9(e)). Within the W/WNW-striking D3 shear zones, the D3 folds are tighter, and the fabrics are transposed subparallel to D3 fabrics (S3) (Figure 9(f)). The superposition of D2 and D3 folds leads to type-3 fold interference structures locally (Figure 9(g)). The D3 shear bands in vertical sections normal to the W/WNW-trending D3 stretching

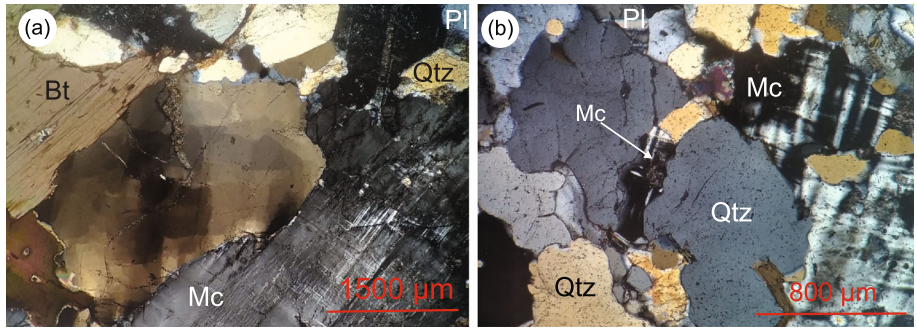

FIGURE 8: Deformation microstructures in granitoids in sections oriented orthogonal to the foliation and parallel to the stretching lineation. (a) Chess-board subgrain structures in quartz in post-D2 pink granitoid. Note iron-grid twinning in a part of large microcline (Mc) crystal. (b) Microfracture in quartz ribbon (symbol Qtz) showing weak strain wavy extinction is filled with aggregates of recrystallized feldspar. The microfracture is oriented orthogonal to the long axis of quartz grain. Other mineral phases marked are biotite (Bt) and plagioclase (Pl).

lineations and fold axes (L3) (see below) indicate persistent N-down kinematics (Figure 9(h)).

3.4. Syntheses of Mesoscale Structures. In the two shallow-dipping domains (Figures 3(a) and 3(b)), the poles to the D2 mylonite foliation (earliest recognizable planar tectonic fabric) in the pre-D2 granitoids constitute a point maximum corresponding to a plane dipping 14° ⟶ 285 N (Figure 4(a)). These D2 foliation planes in the S-L mylonites with down-dip stretching lineations plunging to the west are coplanar with the axial planes of the D2 recumbent/gently-inclined folds in the gneisses (Figure 4(b)). Although data are limited because of the lack of critical outcrops, the hinges of D2 recumbent folds are collinear with the stretching lineations. The axial planes and fold axes of the D2 recumbent to gently inclined folds in the nonanatectic amphibolite facies supracrustal rocks in all the four domains (Figure 4(c)) also overlap with the D2 mylonite fabric and the stretching lineations, respectively, in the granite mylonites (Figure 4(a)). The D2 folds in the anatectic basement gneisses and the nonanatectic supracrustal rocks of low metamorphic grade and the D2 fabrics in the granite mylonites were induced by top-to-the-south thrusting manifested by S-C fabrics and fold vergence in all three lithodemic units (Figure 10(a)).

The anastomosing network of W/WNW-striking steep-dipping D3 fabrics in the granitoids (Figure 4(d)) and the W/WNW trending D3 folds in the basement gneisses (Figure 4(e)) and the supracrustal rocks (Figure 4(f)) are correlated with D3 shear zones characterized by sinistral and north-down kinematics (Figure 4(d)). The progressive tightening of the gently-plunging D3 folds in the neighborhood of the D3 shear zones, and the transposition of the former fabrics within the D3 shear zones, best observed in the supracrustal rocks, testify to this correlation. The hinges of the D3 folds (Figures 4(e) and 4(f)) broadly overlap with the gently-plunging stretching lineations in the steep dipping W-striking D3 mylonite zones (Figure 4(d)).

The mesoscale imbrications and trains of touching euhedral K-feldspar phenocrysts defining steep-dipping fabrics in syn-D3 granitoids are significant [40, 43]. The feature suggests the melt/crystal volume ratio in these granitoids during emplacement was high enough to allow the euhedral K-feldspar phenocrysts to rotate and align themselves [40]. These feldspars describe asymmetric augen locally within the W-striking D3 shears (Figure 7(e)); this implies that the volume fraction of melt in the magma waned considerably either due to melt expulsion and/or rapid cooling in the ascending melts thereby reducing the melt/crystal ratio. Reduction in the ratio induced grain-to-grain contact and caused the feldspar to deform in the solid state. The common occurrence of high-T deformation microstructures in the blastoporphyritic pink granites [28; this study Figure 8(a)] indicates the D3 deformation in the granites occurred at $T > 650^{\circ}$C [41], but the deformation outlasted emplacement and solidification in these granitoids. Finally, the localized occurrence of melt-bearing NNE-striking dextral shears and ENE-striking sinistral shears also suggest local melt pods in the granitoids helped to nucleate the shear zones [43, 45] during the D3 deformation.

In the metatexite basement gneisses, pre-D2 melting is common. But syn-D2 melt productivity in the gneisses was extremely limited and restricted to few biotite-rich gneiss outcrops, and post-D2 anatexis is lacking in both the gneisses (and the supracrustal rocks). The lack of anatexis in the biotite-rich gneisses and the muscovite-biotite bearing supracrustal rocks even in the neighborhood of syn-D3 granitoids suggests that the granitoids cooled below the melting temperature both in the basement and cover rocks [46, 47]. However, this does not preclude the fact that the D3 deformation occurred in a crust being heated by the cooling pre/syn-D3 granitoids.

4. Geochronology

Chronological information on the timing of the different magmato-metamorphic and deformation events in the rocks in the Godhra-Chhota Udepur sector is critical for (a) understanding the tectonic evolution in the area, and (b) correlating the tectonic history with crustal domains to the east and the north of the Godhra-Chhota Udepur sector. In this section, we present U-Pb (zircon) and

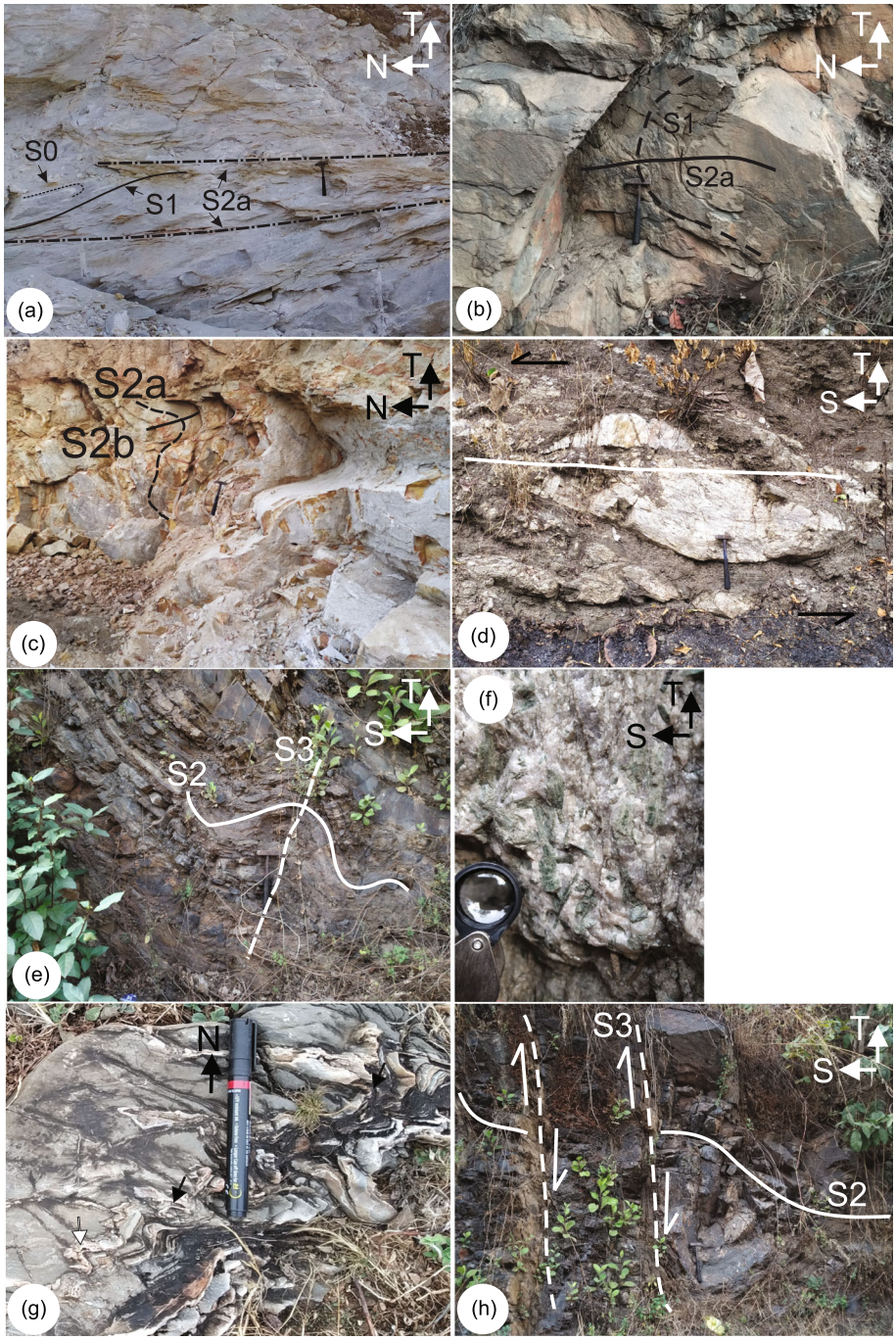

Figure 9: Field photographs of mesoscale structures in supracrustal rocks. (a) Early D1 isoclinal folds on color banding (S0) in meta-carbonate. (b) Round hinged D1 recumbent folds on color banding in meta-arenite. (c) D2 folds on D1 schistosity in micaceous quartzites. (d) D2 top-to-the south transport in shallow-dipping mica schist-quartzite composite. (e) Disharmonic D3 fold on shallow-dipping D2 schistosity in micaceous quartzites. (f) Penetrative steep-dipping D3 axial plane fabric in meta-carbonate (green colored mineral is tremolite). (g) Type-III interference in metacarbonates (hinge of D2 recumbent fold: filled arrow, hinge of D3 fold: open arrow). (h) D3 Shear bands showing N-down sense of movement in micaceous quartzite. Locations of photographs are in Supplementary Material 1.

monazite chemical dates from the basement gneisses, foliated granitoids, and a mica schist from the Champaner Group from the Godhra-Chhota Udepur sector (locations in Figure 3(b)).

4.1. U-Pb Zircon Dating. U-Pb zircon dating was carried out on two samples, anatectic basement gneiss (AW-22) and foliated granite (AW-5). For separating zircons, the samples were crushed and sieved followed by panning to remove the

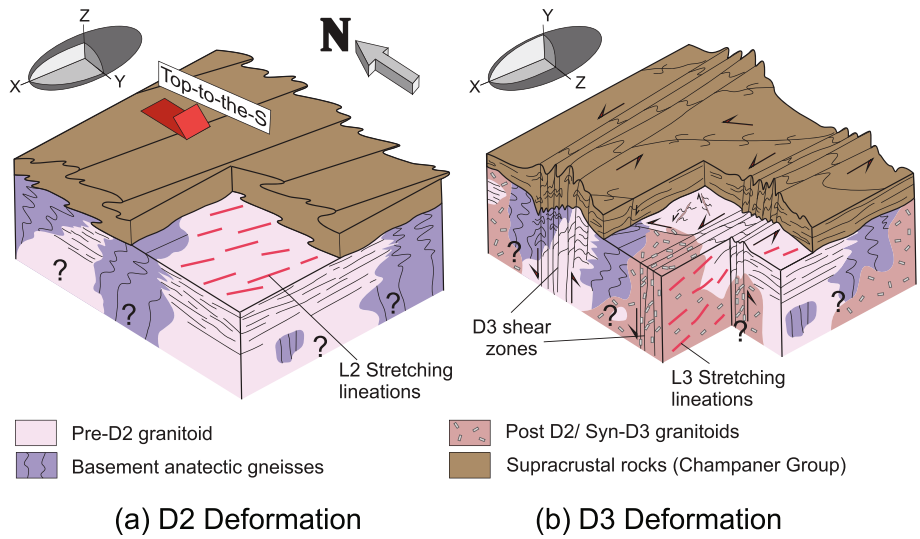

FIGURE 10: Schematic block diagrams displaying the structural development in the Godhra-Chhota Udepur sector during the (a) D2 deformation and (b) D3 deformation events. Strain ellipsoids showing the possible strain axes orientations for each deformation are also shown. The question marks in the block diagrams indicate the uncertainty of the basement structures below the D2 shallow-dipping carapace.

lighter fraction. Heavy liquid and magnetic separations were then performed on the heavier fraction. Finally, the zircon grains were handpicked under a binocular stereomicroscope and mounted in araldite. The mount was then polished to expose the cores of the grains. The zircon grains in both samples are large (~200 μm length, ~50 μm diameter), honey yellow to light brown in color, and transparent to translucent in appearance. The zircon grains are euhedral to subhedral and exhibit luminescent core-rim structures; some grains also show patchy and oscillatory zoning in cathodoluminescence (CL) images taken using the RELION CL instrument at the Plateforme GeOHeLiS, Géosciences Rennes, University of Rennes (Figures 11(a) and 11(c)).

LA-ICP-MS U-Pb analysis of zircons was performed at the Plateforme GeOHeLiS, Géosciences Rennes, University of Rennes using an ESI NWR193UC Excimer laser coupled to an Agilent 7700x, Q-ICP-MS equipped with a dual pumping system to enhance sensitivity. Ablation spot diameters of 25 μm with a repetition rate of 4 Hz and a fluence of 5 J/cm^2 were used. The instrumental condition is detailed in Table 1 [48–51]. Data reduction was performed using Iolite v4 software using U-Pb Geochronology DRS [50]. As the measurement of ^{204}Pb is not precise enough using a Q-ICP-MS, we did not apply a common Pb correction on the data. The presence of common lead can be qualitatively assessed using the f206c indicator which is calculated as follow:

$$f206c = \left(\frac{^{207}\text{Pb}}{^{206}\text{Pb}_m} - \frac{^{207}\text{Pb}}{^{206}\text{Pb}}*\right) / \left(\frac{^{207}\text{Pb}}{^{206}\text{Pb}_c} - \frac{^{207}\text{Pb}}{^{206}\text{Pb}}*\right), \quad (1)$$

where ^{207}Pb/^{206}Pb$_m$ is the measured ratio, ^{207}Pb/^{206}Pb $*$ is the radiogenic expected ratio given a defined age (^{206}Pb/^{238}U age if it is <1000 Ma, ^{207}Pb/^{206}Pb age if not), and ^{207}Pb/^{206}Pb$_c$ is the common Pb ratio based on the Stacey and Kramers [52] Pb evolution model. As this factor relies on assumptions made on the age and on the Pb model, it is only indicative; however, we are confident that the data used for age calculation do not show high level of common Pb.

For individual analyses (Tables 2(a) and 2(b)), the reproducibility of the quality control reference material (Supplementary Material 2) has been propagated by quadratic addition as proposed by [51]. The long-term uncertainty (1.9%) is only applied to population age and is quoted in italics between brackets in the text. All uncertainties are quoted at two sigmas. Concordia diagrams (Figures 11(b) and 11(d)) are generated using IsoplotR [53], and the reported MSWD is for concordance and equivalence. The analytical data for the zircon standard GJ-1 is provided in Supplementary Material 2.

AW-22 (anatectic basement gneiss): the gneiss within the shallow-dipping D2 tectonic mélange is located in the south of the investigated area, outside the bounds of the steep-dipping D3 shear zone (Figures 3 and 4). A total of 45 spots were analyzed in 25 grains from AW-22. The zircon grains mostly exhibit patchy zoning with some grains displaying core-rim structures (Figure 11(a)). Most analyses show Th/U ratios >0.2; two spots, however, have Th/U ratios < 0.1. These spots (Th/U < 0.1) pertain to CL-dark patches in two zircon grains and furnish discordant ages. Concordant analyses are obtained from 11 spots with a Concordia age of 1618 ± 5 (± 62) Ma (MSWD: 1.4, Figure 11(b)). Analyses of another 18 spots plot together with concordant analyses on a Discordia whose upper intercept age is 1672 ± 18 (± 66) Ma.

AW-5 (granite): the blastoporphyritic pink granite is also located within the shallow-dipping carapace (Figure 3); the

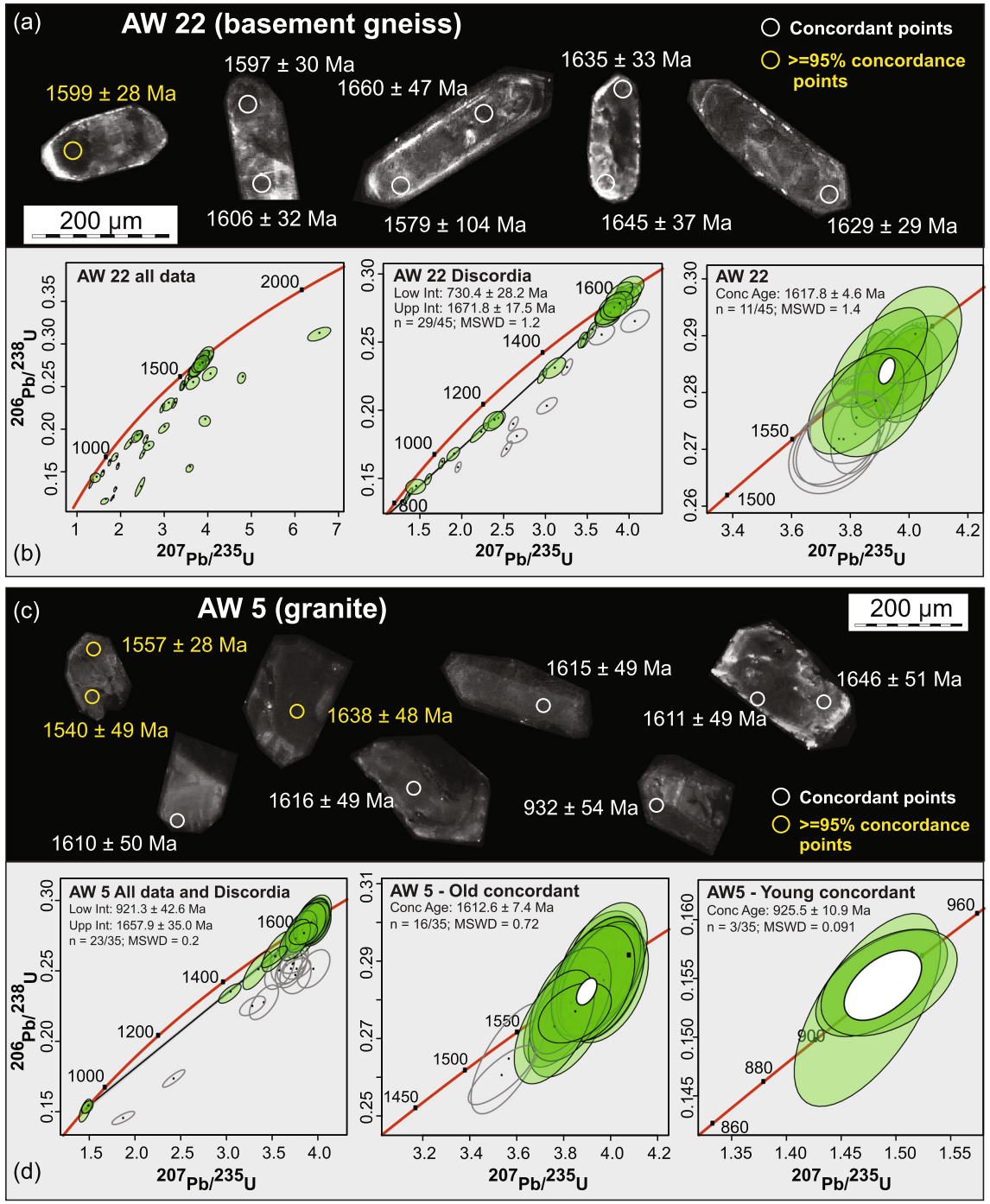

FIGURE 11: (a, c) Representative cathodoluminescence (CL) images of zircon grains in basement gneiss AW-22 and granite AW-5, respectively, showing analyzed U-Pb spots (circled) and their corresponding $^{207}Pb/^{206}Pb$ ages with 2σ errors, (b, d) Zircon U-Pb Concordia plots for the two samples, respectively.

steep-dipping D3 shears are lacking in the granite. A total of 35 spots were analyzed in 25 grains from the foliated granite sample AW-5. The zircon grains mostly show patchy zoning with weakly preserved core-rim structures (Figure 11(c)). All analyses have Th/U ratios > 0.2, except for 5 analyses. These 5 spots (Th/U ~ 0.02 – 0.09) pertain to CL dark domains, and three of them occur as rims on zircon grains and furnish a concordant age of 926 ± 11 (± 37) Ma (MSWD: 0.09). As this age comes from only one grain with a very low MSWD, we consider it as poorly constrained. Another Concordia age population is obtained at 1613 ± 7 (± 62) Ma (16 analyses, MSWD: 0.72) from the cores of the zircon grains. Altogether, and with 4 additional discordant spots, these analyses define

Table 1: Operating conditions for the LA-ICP-MS equipment.

	U-Pb zircon analyses
Laboratory and sample preparation	
Laboratory name	Plateforme GeOHeLiS, Géosciences Rennes/OSUR, Univ. Rennes
Sample type/mineral	Zircon
Sample preparation	Conventional mineral separation, 1-inch araldite mount, 1 μm polish to finish
Imaging	CL: RELION CL instrument, Olympus microscope BX51WI, Leica color camera DFC 420C.
Laser ablation system	
Make, model, and type	ESI NWR193UC, excimer
Ablation cell	ESI NWR TwoVol2
Laser wavelength	193 nm
Pulse width	<5 ns
Fluence	5 J/cm^2
Repetition rate	4 Hz
Spot size	25 μm (round spot)
Sampling mode/pattern	Single spot
Carrier gas	100% He, Ar make-up gas and N_2 (3 ml/min) combined using in-house smoothing device
Background collection	15 seconds
Ablation duration	60 seconds
Wash-out delay	15 seconds
Cell carrier gas flow (he)	0.75 l/min
ICP-MS instrument	
Make, model, and type	Agilent 7700x, Q-ICP-MS
Sample introduction	Via conventional tubing
RF power	1350 W
Sampler, skimmer cones	Ni
Extraction lenses	X type
Make-up gas flow (Ar)	0.75 l/min
Detection system	Single collector secondary electron multiplier
Data acquisition protocol	Time-resolved analysis
Scanning mode	Peak hopping, one point per peak
Detector mode	Pulse counting, dead time correction applied, and analog mode when signal intensity > ~ 10^6 cps
Masses measured	^{204}(Hg + Pb), ^{206}Pb, ^{207}Pb, ^{208}Pb, ^{232}Th, ^{238}U
Integration time per peak	10-30 ms
Sensitivity/efficiency	28000 cps/ppm Pb (50 μm, 10 Hz)
Dwell time per isotope	10-30 ms depending on the masses
Data processing	
Calibration strategy	91500 zircon used as primary reference material, GJ-1 zircon used as secondary reference material (quality control)
Reference material info	91500 [48] GJ-1 [49]
Data processing package used	Iolite v.4.4, U-Pb Geochronology DRS [50]
Mass discrimination	Standard-sample bracketing with ^{207}Pb/^{206}Pb and ^{206}Pb/^{238}U normalized to reference material 91500
Common Pb correction	No common Pb correction
Uncertainty level and propagation	Ages are quoted at 2 sigma, propagation is by quadratic addition according to [51].
Quality control/validation	GJ-1, Concordia age = 603.2 ± 2.3 Ma (n = 14; MSWD = 1.8)

a Discordia that yields an upper intercept age of 1658 ± 35 (± 72) Ma and a lower intercept age of 921 ± 43 (± 55) Ma (Figure 11(d)).

4.2. Monazite Chemical Dating. In this study, monazites in four samples were analyzed by electron microprobe dating [54] in the Department of Earth Sciences, Indian Institute of Technology, Bombay (Powai). The protocol for monazite analyses is detailed in [55], and only a brief summary is presented here. The analyses were performed with a focused beam (~1 μm diameter), the accelerating voltage was 15 kV, and the beam current was 200 nA. Th, U, and Pb were analyzed using the ThM_a, UM_b, and PbM_a X-ray lines simultaneously on two LPET crystals with peak counting times of 160 s, 160 s, and 240 s, respectively. Background measurements were made with half the peak time. The peak and background acquisitions for Pb were done using the PbM_a peak position based on a two-point exponential fit following the suggestions of [56]. This is in contrast to a multipoint exponential fit [57, 58] that produces statistically meaningful background values for Pb and reduces the uncertainties in the chemical dates obtained from monazites by tens of millions of years. For our samples, we have adopted the two-point exponential fit method, and the measured intensities for PbM_a were corrected for ThM2-O4, ThMζ1, ThMζ2, YL_{C2}, YL_{C3}, and LaL_a interferences. Also, samples were chosen such that the abundances of the elements ThO_2 (3.35–17.43 wt%), UO_2 (0.01–1.40 wt%), PbO (0.17–0.77 wt%), and Y_2O_3 (0.21–3.03 wt%) were high to keep errors in background measurement low; only spots with 2σ errors < 8% error$(100 \times 2\sigma \text{errors/totalage in Ma})$ [59] were considered.

The Th-U-Pb (total) chemical dates in monazites were obtained following the formulation of Montel et al. [54]. Based on X-ray element maps Th, U, Pb, and Y (Figure 12) and back-scattered electron images, 80 spot dates in chemically distinct domains were analyzed in the samples, e.g., basement anatectic gneiss (AW-142), a biotite-rich gneiss enclave within grey-colored granitoid (AW-77B),

Table 2: U-Pb zircon analytical data for samples (a) AW-22 (basement gneisses) and (b) AW-5 (foliated granite), locations in Figure 3. Lines in bold and italics are discordant analyses, and lines in bold are concordant analyses.

(a) U-Pb zircon analytical data for sample AW 22 (basement gneiss)

GeOHeLiS platform, Universite Rennes 1						Data for Tera-Wasserburg plot					Data for Wetherill plot					Dates						
Identifier	f206c	^{206}Pb (cps)	Uppm	Th/U	Pbppm	^{238}U/^{206}Pb	2se%	^{207}Pb/^{206}Pb	2se%	Rho	^{207}Pb/^{235}U	2se%	^{206}Pb/^{238}U	2se%	Rho	^{207}Pb/^{206}Pb	2se (abs)	^{206}Pb/^{238}U	2se (abs)	^{207}Pb/^{235}U	2se (abs)	% conc
AW22_1	2.2	152623	794	0.11	93	6.31	2.0	0.08913	1.6	0.15	1.9530	1.5	0.15843	2.0	0.58	1406	31	948	17	1099	10	86.2
AW22_2	**0.0**	**67864**	**193**	**0.65**	**100**	**3.52**	**1.9**	**0.09861**	**1.6**	**0.39**	**3.8834**	**1.4**	**0.28432**	**1.9**	**0.38**	**1597**	**30**	**1613**	**27**	**1610**	**11**	**100.8**
AW22_3	**0.0**	**76580**	**223**	**0.77**	**132**	**3.56**	**2.0**	**0.09910**	**1.7**	**0.33**	**3.8802**	**1.6**	**0.28100**	**2.0**	**0.48**	**1606**	**32**	**1596**	**28**	**1610**	**13**	**100.2**
AW22_4	20.3	49985	754	0.05	264	7.50	6.9	0.23356	5.4	0.80	2.4724	3.7	0.13331	6.9	0.88	3076	87	807	53	1264	27	63.8
AW22_5	***0.6***	***2734479***	***15564***	***1.39***	***7994***	***7.24***	***3.4***	***0.07156***	***2.0***	***0.06***	***1.3678***	***3.3***	***0.13808***	***3.4***	***0.89***	***973***	***41***	***834***	***27***	***875***	***19***	***95.3***
AW22_6	5.7	275221	1929	0.55	526	8.31	2.5	0.11062	1.5	0.03	1.8412	2.0	0.12039	2.5	0.91	1809	28	733	18	1060	13	69.1
AW22_7	***0.0***	***100986***	***362***	***0.43***	***153***	***4.43***	***2.0***	***0.09502***	***1.6***	***0.12***	***2.9777***	***1.5***	***0.22582***	***2.0***	***0.68***	***1528***	***30***	***1313***	***24***	***1402***	***12***	***91.8***
AW22_8	**0.0**	**109289**	**328**	**0.72**	**176**	**3.52**	**2.0**	**0.09860**	**1.7**	**0.43**	**3.8881**	**1.5**	**0.28438**	**2.0**	**0.50**	**1597**	**32**	**1613**	**29**	**1611**	**12**	**100.9**
AW22_9	0.0	72600	326	0.44	102	5.26	2.2	0.09901	1.8	0.34	2.6124	1.8	0.19020	2.2	0.66	1605	33	1122	23	1304	13	81.3
AW22_10	0.0	74378	199	0.75	243	3.19	2.1	0.14818	2.8	-0.37	6.5612	3.3	0.31332	2.1	0.57	2324	48	1757	32	2054	29	88.4
AW22_11	11.9	272368	1507	0.39	963	6.39	2.4	0.16956	2.2	0.61	3.5979	1.9	0.15659	2.4	0.35	2553	37	938	21	1549	15	60.5
AW22_12	***0.0***	***158602***	***525***	***0.66***	***256***	***3.97***	***1.9***	***0.09932***	***1.5***	***0.44***	***3.4789***	***1.3***	***0.25216***	***1.9***	***0.67***	***1610***	***28***	***1450***	***25***	***1522***	***10***	***94.5***
AW22_13	0.0	112825	462	0.46	274	4.71	2.4	0.13629	3.2	0.45	3.9457	2.7	0.21220	2.4	0.02	2180	55	1241	27	1623	22	74.5
AW22_14	0.0	69770	253	0.60	118	4.31	2.1	0.10109	1.6	0.23	3.2543	1.6	0.23183	2.1	0.69	1643	30	1344	25	1470	13	89.5
AW22_15	**0.0**	**81714**	**240**	**0.68**	**130**	**3.53**	**1.9**	**0.10033**	**1.6**	**0.46**	**3.9432**	**1.3**	**0.28315**	**1.9**	**0.37**	**1629**	**29**	**1607**	**27**	**1623**	**11**	**99.6**
AW22_16	**0.0**	**88113**	**262**	**0.45**	**122**	**3.51**	**2.0**	**0.10065**	**1.8**	**0.46**	**3.9842**	**1.5**	**0.28509**	**2.0**	**0.39**	**1635**	**33**	**1617**	**29**	**1631**	**12**	**99.7**
AW22_17	***0.0***	***115182***	***379***	***0.68***	***200***	***3.67***	***2.1***	***0.10120***	***2.0***	***0.24***	***3.8147***	***1.8***	***0.27273***	***2.1***	***0.33***	***1645***	***37***	***1555***	***29***	***1596***	***14***	***97.0***
AW22_18	***0.8***	***180728***	***886***	***0.11***	***94***	***6.15***	***2.0***	***0.07851***	***1.7***	***0.24***	***1.7655***	***1.6***	***0.16256***	***2.0***	***0.56***	***1159***	***34***	***971***	***18***	***1033***	***10***	***94.0***
AW22_19	***0.0***	***199281***	***639***	***1.11***	***543***	***3.85***	***1.9***	***0.09864***	***1.5***	***0.50***	***3.5584***	***1.2***	***0.25973***	***1.9***	***0.58***	***1598***	***27***	***1488***	***25***	***1540***	***10***	***96.4***
AW22_20	0.0	72087	229	0.75	221	3.81	2.0	0.13497	2.0	1.00	4.8063	1.6	0.26221	2.0	0.23	2163	35	1501	27	1786	13	82.6
AW22_21	4.8	343738	2141	0.58	507	7.63	2.0	0.10493	1.5	0.59	1.9086	1.3	0.13108	2.0	0.63	1712	28	794	15	1084	9	73.2
AW22_22	**0.0**	**48363**	**135**	**0.64**	**79**	**3.53**	**2.4**	**0.10200**	**2.5**	**0.38**	**3.9996**	**2.4**	**0.28330**	**2.4**	**0.33**	**1660**	**47**	**1608**	**35**	**1634**	**20**	**98.4**
AW22_23	***0.9***	***101097***	***605***	***0.08***	***34***	***6.64***	***2.2***	***0.07704***	***2.0***	***0.33***	***1.6009***	***2.0***	***0.15055***	***2.2***	***0.51***	***1121***	***40***	***904***	***19***	***971***	***13***	***93.1***
AW22_24	***0.0***	***121282***	***398***	***0.66***	***199***	***3.96***	***1.9***	***0.09872***	***1.5***	***0.54***	***3.4520***	***1.3***	***0.25272***	***1.9***	***0.58***	***1599***	***28***	***1452***	***25***	***1516***	***10***	***94.8***
AW22_25	0.0	102905	480	0.39	205	5.82	2.7	0.10710	1.8	0.48	2.5321	2.1	0.17184	2.7	0.81	1750	33	1022	25	1281	15	73.2
AW22_26	***0.0***	***146076***	***843***	***0.37***	***240***	***5.14***	***2.7***	***0.09522***	***5.6***	***0.44***	***2.4356***	***3.5***	***0.19456***	***2.7***	***0.49***	***1531***	***106***	***1146***	***28***	***1253***	***25***	***81.8***
AW22_27	0.0	101504	411	0.67	221	3.91	2.4	0.10207	5.5	0.53	3.6683	3.4	0.25564	2.4	0.48	1661	102	1468	32	1564	27	94.2
AW22_28	***0.0***	***151629***	***964***	***0.16***	***114***	***5.94***	***2.4***	***0.08302***	***5.5***	***0.36***	***1.9076***	***3.3***	***0.16832***	***2.4***	***0.55***	***1269***	***107***	***1003***	***22***	***1084***	***22***	***85.4***
AW22_29	***0.0***	***317246***	***1852***	***0.37***	***594***	***5.42***	***3.2***	***0.08899***	***5.6***	***0.16***	***2.2306***	***4.0***	***0.18445***	***3.2***	***0.84***	***1403***	***107***	***1091***	***32***	***1191***	***28***	***84.9***
AW22_30	**0.0**	**113947**	**415**	**0.67**	**223**	**3.51**	**2.6**	**0.09858**	**5.6**	**0.44**	**3.9957**	**3.5**	**0.28473**	**2.6**	**0.50**	**1597**	**105**	**1615**	**37**	**1633**	**29**	**102.3**
AW22_31	0.0	130307	690	0.21	157	4.92	2.4	0.10763	5.5	0.28	3.0139	3.3	0.20346	2.4	0.65	1759	100	1194	27	1411	25	80.2
AW22_32	**0.0**	**55370**	**203**	**0.87**	**136**	**3.44**	**2.4**	**0.09859**	**5.5**	**0.44**	**4.0189**	**3.3**	**0.29034**	**2.4**	**0.32**	**1597**	**103**	**1643**	**34**	**1638**	**27**	**102.6**
AW22_33	***0.0***	***75943***	***417***	***0.24***	***87***	***5.17***	***3.0***	***0.08688***	***5.8***	***0.19***	***2.3890***	***4.1***	***0.19333***	***3.0***	***0.42***	***1357***	***113***	***1139***	***31***	***1239***	***29***	***91.3***
AW22_34	**0.0**	**164437**	**621**	**0.76**	**369**	**3.49**	**2.5**	**0.09641**	**5.5**	**0.40**	**3.9027**	**3.4**	**0.28642**	**2.5**	**0.62**	**1555**	**103**	**1624**	**35**	**1614**	**27**	**103.8**
AW22_35	**0.0**	**69528**	**270**	**0.67**	**140**	**3.59**	**2.6**	**0.09588**	**5.6**	**0.47**	**3.8181**	**3.5**	**0.27827**	**2.6**	**0.51**	**1545**	**105**	**1583**	**36**	**1597**	**28**	**103.4**
AW22_36	***0.0***	***81601***	***367***	***0.60***	***183***	***3.70***	***2.4***	***0.10323***	***5.5***	***0.49***	***3.7436***	***3.4***	***0.27017***	***2.4***	***0.34***	***1682***	***103***	***1542***	***33***	***1581***	***27***	***94.0***

Table 2: Continued.

GeOHeLiS platform, Universite Rennes 1						Data for Tera-Wasserburg plot					Data for Wetherill plot							Dates				
Identifier	f206c	^{206}Pb (cps)	Uppm	Th/U	Pbppm	^{238}U/^{206}Pb	2se%	^{207}Pb/^{206}Pb	2se%	Rho	^{207}Pb/^{235}U	2se%	^{206}Pb/^{238}U	2se%	Rho	^{207}Pb/^{206}Pb	2se (abs)	^{206}Pb/^{238}U	2se (abs)	^{207}Pb/^{235}U	2se (abs)	% conc
AW22_37	0.0	120922	559	0.67	387	3.77	2.5	0.11290	5.5	0.48	4.0642	3.4	0.26555	2.5	0.48	1846	100	1518	34	1647	28	89.2
AW22_38	***0.0***	***326665***	***1508***	***0.82***	***1054***	***3.68***	***2.4***	***0.10199***	***5.5***	***0.34***	***3.7597***	***3.4***	***0.27188***	***2.4***	***0.48***	***1660***	***101***	***1550***	***33***	***1584***	***27***	***95.4***
AW22_39	0.0	97071	679	0.31	243	5.52	2.4	0.10837	5.6	-0.10	2.6558	3.7	0.18127	2.4	0.44	1771	103	1074	24	1316	27	74.3
AW22_40	***2.0***	***179089***	***1628***	***0.10***	***173***	***6.92***	***3.1***	***0.08489***	***5.9***	***0.52***	***1.4546***	***6.7***	***0.14460***	***3.1***	***0.13***	***1312***	***115***	***871***	***25***	***912***	***41***	***95.5***
AW22_41	***0.0***	***55589***	***244***	***0.79***	***150***	***3.68***	***2.5***	***0.09739***	***5.6***	***0.39***	***3.7749***	***3.5***	***0.27184***	***2.5***	***0.46***	***1574***	***105***	***1550***	***34***	***1587***	***28***	***100.9***
AW22_42	***0.0***	***40333***	***175***	***0.59***	***81***	***3.63***	***2.4***	***0.09768***	***5.6***	***0.45***	***3.8188***	***3.4***	***0.27562***	***2.4***	***0.33***	***1579***	***104***	***1569***	***34***	***1597***	***28***	***101.1***
AW22_43	***0.0***	***128235***	***702***	***0.63***	***334***	***4.32***	***2.7***	***0.10071***	***5.6***	***0.45***	***3.1095***	***3.6***	***0.23135***	***2.7***	***0.53***	***1636***	***104***	***1342***	***33***	***1435***	***27***	***87.7***
AW22_44	4.8	101978	1063	0.02	137	8.44	2.5	0.10258	6.0	0.02	1.6674	4.4	0.11848	2.5	0.44	1671	112	722	17	996	28	72.5
AW22_45	**0.0**	**54332**	**233**	**0.93**	**172**	**3.59**	**2.8**	**0.10126**	**5.8**	**0.52**	**3.8846**	**3.7**	**0.27859**	**2.8**	**0.36**	**1647**	**107**	**1584**	**39**	**1610**	**30**	**97.8**

f206% = (^{207}Pb/^{206}Pb$_m$ − ^{207}Pb/^{206}Pb ∗)/(^{207}Pb/^{206}Pb$_c$ − ^{207}Pb/^{206}Pb ∗) × 100 (see text for further explanation). If Age^{206}Pb/^{238}U < 1000 Ma concordance% = (Age^{206}Pb/^{238}U/Age^{207}Pb/^{235}U) ∗ 100; else concordance% = (Age^{207}Pb/^{235}U/Age^{207}Pb/^{206}Pb) ∗ 100. Uncertainties include secondary standard uncertainty propagation as proposed by Horstwood et al. [51].

(b) U-Pb zircon analytical data for sample AW 5 (granite)

GeOHeLiS platform, Universite Rennes 1						Data for Tera-Wasserburg plot					Data for Wetherill plot							Dates				
Identifier	f206c	^{206}Pb (cps)	Uppm	Th/U	Pbppm	^{238}U/^{206}Pb	2se%	^{207}Pb/^{206}Pb	2se%	Rho	^{207}Pb/^{235}U	2se%	^{206}Pb/^{238}U	2se%	Rho	^{207}Pb/^{206}Pb	2se (abs)	^{206}Pb/^{238}U	2se (abs)	^{207}Pb/^{235}U	2se (abs)	% conc
AW5_1	***0.0***	***356047***	***1439***	***0.55***	***657***	***3.98***	***4.4***	***0.09566***	***2.6***	***0.34***	***3.3507***	***3.8***	***0.25156***	***4.4***	***0.73***	***1540***	***49***	***1447***	***57***	***1493***	***29***	***96.9***
AW5_2	0.0	79741	331	0.80	202	3.97	4.4	0.11352	2.6	0.58	3.9508	3.7	0.25180	4.4	0.48	1856	48	1448	57	1624	30	87.5
AW5_3	0.0	131543	603	0.53	261	4.39	4.4	0.10799	2.7	0.43	3.4092	3.8	0.22804	4.4	0.62	1765	49	1324	53	1507	30	85.4
AW5_4	0.0	106936	428	0.67	229	3.99	4.4	0.10307	2.6	0.51	3.5796	3.7	0.25071	4.4	0.51	1679	49	1442	57	1545	30	92.0
AW5_5	**0.0**	**53401**	**184**	**0.68**	**92**	**3.48**	**4.4**	**0.09927**	**2.7**	**0.41**	**3.9563**	**3.8**	**0.28775**	**4.4**	**0.39**	**1610**	**50**	**1630**	**63**	**1625**	**31**	**101.0**
AW5_6	**0.0**	**114999**	**387**	**0.68**	**202**	**3.51**	**4.3**	**0.09999**	**2.7**	**0.50**	**3.9559**	**3.8**	**0.28498**	**4.3**	**0.39**	**1623**	**50**	**1616**	**62**	**1625**	**30**	**100.1**
AW5_7	***0.0***	***224542***	***790***	***0.83***	***474***	***3.60***	***4.3***	***0.09919***	***2.6***	***0.48***	***3.8036***	***3.7***	***0.27775***	***4.3***	***0.60***	***1608***	***48***	***1580***	***61***	***1594***	***30***	***99.1***
AW5_8	0.0	111344	441	0.66	201	3.93	4.4	0.10446	2.7	0.21	3.6572	3.8	0.25431	4.4	0.26	1704	51	1461	58	1562	30	91.7
AW5_9	**0.0**	**121536**	**397**	**0.74**	**221**	**3.49**	**4.4**	**0.09953**	**2.6**	**0.40**	**3.9498**	**3.7**	**0.28646**	**4.4**	**0.49**	**1615**	**49**	**1624**	**63**	**1624**	**30**	**100.6**
AW5_10	0.0	108541	400	0.56	187	3.92	4.4	0.10571	2.6	0.41	3.7235	3.7	0.25528	4.4	0.50	1726	48	1466	57	1576	30	91.3
AW5_11	***0.0***	***180374***	***607***	***0.75***	***322***	***3.63***	***4.4***	***0.10079***	***2.6***	***0.54***	***3.8260***	***3.7***	***0.27534***	***4.4***	***0.53***	***1638***	***48***	***1568***	***61***	***1598***	***30***	***97.6***
AW5_12	0.0	42748	161	0.47	63	3.97	4.4	0.10709	2.7	0.49	3.7057	3.8	0.25193	4.4	0.49	1750	50	1448	58	1573	31	89.9
AW5_13	***0.1***	***396569***	***2429***	***0.02***	***24***	***6.56***	***4.4***	***0.07016***	***2.6***	***0.49***	***1.4744***	***3.7***	***0.15252***	***4.4***	***0.64***	***932***	***54***	***915***	***37***	***920***	***23***	***99.5***
AW5_14	**0.0**	**221010**	**712**	**0.73**	**385**	**3.49**	**4.4**	**0.09960**	**2.6**	**0.51**	**3.9290**	**3.7**	**0.28668**	**4.4**	**0.58**	**1616**	**49**	**1625**	**63**	**1620**	**30**	**100.2**
AW5_15	0.0	236459	837	0.62	461	4.04	4.4	0.10964	2.7	0.61	3.7537	3.7	0.24743	4.4	0.22	1793	50	1425	56	1583	30	88.3
AW5_16	***0.0***	***304945***	***1026***	***0.67***	***504***	***3.55***	***4.5***	***0.09926***	***2.6***	***0.49***	***3.8488***	***3.8***	***0.28191***	***4.5***	***0.67***	***1609***	***49***	***1601***	***63***	***1603***	***30***	***99.6***
AW5_17	**0.0**	**85975**	**283**	**0.73**	**155**	**3.49**	**4.4**	**0.10017**	**2.7**	**0.40**	**3.9387**	**3.8**	**0.28619**	**4.4**	**0.50**	**1626**	**51**	**1622**	**64**	**1622**	**31**	**99.7**
AW5_18	***0.0***	***254350***	***894***	***0.72***	***462***	***3.77***	***4.4***	***0.09707***	***2.6***	***0.31***	***3.5653***	***3.7***	***0.26494***	***4.4***	***0.71***	***1568***	***48***	***1515***	***59***	***1542***	***30***	***98.4***
AW5_19	**0.0**	**110160**	**370**	**0.62**	**171**	**3.52**	**4.4**	**0.10122**	**2.7**	**0.50**	**3.9752**	**3.8**	**0.28447**	**4.4**	**0.37**	**1646**	**51**	**1614**	**63**	**1629**	**31**	**99.0**
AW5_20	**0.0**	**150316**	**500**	**0.73**	**275**	**3.45**	**4.4**	**0.09932**	**2.6**	**0.49**	**3.9765**	**3.7**	**0.28982**	**4.4**	**0.44**	**1611**	**49**	**1641**	**63**	**1629**	**30**	**101.2**
AW5_21	**0.0**	**146576**	**764**	**0.78**	**697**	**3.49**	**4.4**	**0.09899**	**2.6**	**0.51**	**3.9506**	**3.7**	**0.28673**	**4.4**	**0.48**	**1604**	**48**	**1625**	**63**	**1624**	**30**	**101.2**
AW5_22	**0.0**	**144247**	**790**	**0.89**	**872**	**3.51**	**4.4**	**0.10018**	**2.6**	**0.53**	**3.9686**	**3.7**	**0.28518**	**4.4**	**0.45**	**1627**	**49**	**1617**	**63**	**1628**	**30**	**100.1**

Table 2: Continued.

GeOHeLiS platform, Universite Rennes 1						Data for Tera-Wasserburg plot					Data for Wetherill plot					Dates						
Identifier	f206c	^{206}Pb (cps)	Uppm	Th/U	Pbppm	^{238}U/^{206}Pb	2se%	^{207}Pb/^{206}Pb	2se%	Rho	^{207}Pb/^{235}U	2se%	^{206}Pb/^{238}U	2se%	Rho	^{207}Pb/^{206}Pb	2se (abs)	^{206}Pb/^{238}U	2se (abs)	^{207}Pb/^{235}U	2se (abs)	% conc
AW5_23	***0.0***	***169452***	***958***	***0.75***	***874***	***3.58***	***4.3***	***0.09853***	***2.6***	***0.91***	***3.8303***	***3.7***	***0.27936***	***4.3***	***0.48***	***1596***	***48***	***1588***	***61***	***1599***	***30***	***100.2***
AW5_24	**0.0**	**211002**	**1153**	**0.95**	**1386**	**3.51**	**4.3**	**0.09869**	**2.6**	**0.50**	**3.9308**	**3.7**	**0.28461**	**4.3**	**0.38**	**1599**	**48**	**1615**	**62**	**1620**	**30**	**101.3**
AW5_25	***0.0***	***317370***	***1767***	***0.69***	***1480***	***3.66***	***4.4***	***0.09830***	***2.6***	***0.40***	***3.7597***	***3.7***	***0.27323***	***4.4***	***0.56***	***1591***	***49***	***1557***	***61***	***1584***	***30***	***99.6***
AW5_26	***0.0***	***479789***	***1621***	***0.83***	***942***	***3.84***	***2.4***	***0.09651***	***5.4***	***0.35***	***3.5350***	***3.3***	***0.26070***	***2.4***	***0.79***	***1557***	***102***	***1493***	***32***	***1535***	***26***	***98.6***
AW5_27	***0.0***	***182114***	***729***	***0.51***	***250***	***4.24***	***2.4***	***0.09542***	***5.5***	***0.51***	***3.0466***	***3.3***	***0.23568***	***2.4***	***0.71***	***1536***	***103***	***1364***	***30***	***1419***	***25***	***92.4***
AW5_28	**0.1**	**312447**	**1898**	**0.02**	**28**	**6.47**	**2.4**	**0.07047**	**5.5**	**0.47**	**1.4881**	**3.3**	**0.15465**	**2.4**	**0.55**	**941**	**112**	**927**	**20**	**926**	**20**	**100.2**
AW5_29	**0.3**	**353015**	**2223**	**0.02**	**41**	**6.46**	**2.4**	**0.07210**	**5.5**	**0.45**	**1.4940**	**3.4**	**0.15485**	**2.4**	**0.43**	**988**	**112**	**928**	**21**	**928**	**21**	**100.0**
AW5_30	0.0	140091	617	0.49	226	4.43	2.5	0.10986	5.5	0.44	3.2839	3.5	0.22549	2.5	0.58	1796	100	1311	30	1477	27	82.2
AW5_31	**0.0**	**156248**	**536**	**0.67**	**245**	**3.61**	**2.3**	**0.09962**	**5.5**	**0.44**	**3.8484**	**3.3**	**0.27715**	**2.3**	**0.40**	**1616**	**102**	**1577**	**32**	**1603**	**26**	**99.2**
AW5_32	3.2	320014	2285	0.08	240	6.85	2.6	0.09526	6.0	-0.53	1.8721	5.4	0.14596	2.6	0.79	1532	112	878	21	1071	35	82.0
AW5_33	0.0	117642	463	0.59	213	3.97	2.4	0.11024	5.5	0.54	3.7682	3.3	0.25185	2.4	0.40	1803	100	1448	31	1586	26	88.0
AW5_34	0.0	71406	273	0.57	111	3.91	2.3	0.10646	5.5	0.45	3.7331	3.3	0.25572	2.3	0.36	1739	100	1468	30	1578	26	90.8
AW5_35	0.0	238566	1512	0.09	250	5.75	2.9	0.09987	5.5	-0.15	2.4237	4.1	0.17396	2.9	0.87	1621	103	1034	28	1250	30	77.1

f206% = (^{207}Pb/^{206}Pb$_m$ − ^{207}Pb/^{206}Pb ∗)/(^{207}Pb/^{206}Pb$_c$ − ^{207}Pb/^{206}Pb ∗) × 100 (see text for further explanation). If Age^{206}Pb/^{238}U < 1000 Ma concordance% = (Age^{206}Pb/^{238}U/Age^{207}Pb/^{235}U) ∗ 100; else concordance% = (Age^{207}Pb/^{235}U/Age^{207}Pb/^{206}Pb) ∗ 100. Uncertainties include secondary standard uncertainty propagation as proposed by Horstwood et al. [51].

muscovite-biotite schist within the supracrustal unit (AW-82A), and pink granitoid with steep-dipping D3 fabrics (AW-16). A brief description of the rocks, textural-chemical characteristics, and summary dates in monazite are provided in Table 3. The mean population ages were statistically resolved using Isoplot 3.0 [60]. The spot ages were calibrated against the monazite standard Steenkampskraal (SHRIMP age 1030 ± 6 Ma) [61]. Monazite analytical data and spot ages (±2σ errors) are presented in Supplementary Material 3 [62].

In the samples, monazite grains are common within mica aggregates and are rarely observed in quartz-feldspar rich domains. The analyzed monazites occur as ellipsoidal to prismatic grains xenoblastic to subidioblastic in shape (Figures 12(a)–12(d)). The long axis of the monazites in the gneisses and granites was > 20 μm, and up to 50 μm in rare grains (Figure 12). Out of 35 meta-argillaceous/arenaceous supracrustal rocks, monazites were identified in only one sample (AW-82A) with grains typically ~10 um in length. The monazites in the four samples are of two textural types, i.e., monazites nebulously and concentrically zoned in Th, Y, U, and rarely Pb, and chemically homogenous monazites (Figure 12). In total, 74 spots were analyzed in the four samples (Supplementary Material 3). Monazite spot ages in all the samples taken together varied between 905 ± 35 Ma and 1059 ± 71 Ma (Table 3, Supplementary Material 3). The error%[100 x (2σ error in Ma)/(absolute age in Ma)] per spot is less than 5%, except for 3 spot ages (6.2%, 5.1%, and 5.2%) in AW-142, and between 5.38 and 13.8 in 9 out of 10 spots in the mica schist AW-82A (Supplementary Material 3). The error% increases with decreasing ThO_2 and PbO contents, but is weakly correlated with UO_2 and Y_2O_3 contents (cf. Prabhakar [62]).

Seventeen spot dates in the anatectic gneiss AW-142 yield a mean population date of 905 ± 9 Ma (MSWD = 0.59) (Figure 12(a)). The 23 spot dates in the anatectic gneiss (AW-77B) occurring as an enclave within a foliated granite are resolved into two populations with mean dates of 947 ± 12 Ma (MSWD = 0.63) and a subsidiary peak at 1005 ± 15 Ma (MSWD = 2.1) (Figure 12(b)). By contrast, the statistically-resolved mean population dates obtained from 25 spots in the foliated granite (AW-16) are 912 ± 12 Ma (MSWD = 0.27) and 974 ± 11 Ma (MSWD = 2.1) (Figure 12(c)). And finally, the 10 spot dates in muscovite-schist AW-82A neighboring Jambughoda in the Champaner Group are resolved into a single age population with the mean age of 972 ± 31 Ma (MSWD = 1.7) (Figure 12(d)).

5. Discussion

5.1. Kinematics of Deformation in the Godhra-Chhota Udepur Sector. In this section, we summarize several crucial aspects in the Godhra-Chhota Udepur sector that are conspicuous from an analysis of the mesoscale and regional structures (Figure 10). First, the D2 stretching lineations in granitoids, and the hinges of recumbent to gently-inclined tight folds in the basement gneisses (Figures 4(a) and 4(b)) and the lower grade supracrustal rocks (Figure 4(c)) in the shallow-dipping tectonic mélange are broadly collinear. Second, top-to-the south overthrusting resulted in the D2 folding in the supracrustal rocks and the gneisses that are interleaved with pre-D2 granitoid mylonites; the axial planes of D2 folds are coplanar with the earliest tectonic fabric in the grey granitoids (Figure 4(b)). Third, the D3 stretching lineations in granitoids (Figure 4(d)) and the hinges of upright to steeply-inclined gently-plunging tight to open folds in the gneisses (Figure 4(e)) and the supracrustal rocks are broadly collinear (Figure 4(f)). Fourth, the W/WNW-plunging stretching lineations in the D2 shallow-dipping tectonic nappes (Figure 4(b)) and in the steep-dipping W/WNW-striking shear zones (Figure 4(e)) that dissect the carapace share a low-angle obliquity. And finally, the D3 deformation was broadly contemporaneous with the emplacement of pink blastoporphyritic granitoids, but in most cases, the deformation outlasted solidification in the granitoids.

Any kinematic model for deformation in the Precambrian rocks in the area needs to account for these attributes of planar and linear structures. Several authors have addressed the issue of colinearity of fold hinges and stretching lineations both parallel and oblique to the slip direction [63–69]. The colinearity may result from the progressive rotation of hinges of contemporary folds that formed initially oblique to the extension direction of the strain ellipsoid [69, 70]. Alternatively fold hinges subparallel to stretching lineations may nucleate as a consequence of shearing [68, 71, 72]. The D2 stretching lineations (x-axis of the strain ellipsoid) in the two domains of the shallow-dipping carapace (XY plane) of the Godhra-Chhota Udepur sector (Figures 3(a), 3(b), and 10(a)) were determined in granite mylonites. The mylonite fabric, demonstrably axial planar to the recumbent/gently-inclined D2 folds in the basement gneisses, is the first recognizable tectonic fabric in the granites that otherwise do not preserve any preexisting tectonic fabric. In addition, the lack of wide variations in the orientations of the D2 fold hinges in the gneisses (Figure 4(b)) and the supracrustal rocks (Figure 4(c)), and the stretching lineations (Figure 4(a)) suggest the colinearity of the fold hinges and the stretching lineations were not formed by the progressive rotation of the early formed folds towards the x-axis. Instead, the persistent top-to-the-south sense of movement on D2 foliation surfaces both in the allochthonous supracrustal rocks and in the gneisses was caused by basement involved thrust tectonics involving N-S shortening (Figure 10(a)).

The subvertical E-striking D3 shear zones with persistent sinistral and N-down kinematics exhibit W/WNW-trending moderately-plunging stretching lineations (Figure 10(b)). In transtensional shear zones, folds typically originate at angles >45° to the shear plane and are subsequently rotated towards the orientation of the divergence vector. In contrast, the folds induced by transpressional deformation form at angles <45° to the XY plane, but rotate towards the shear zone with increasing strain [72]. It stands to reason therefore that the low-angle obliquity between the D3 fold hinges in the basement gneisses/supracrustal rocks, and the D3 stretching lineations (x-axis) (Figure 10(b)) was the result of transpressional deformation. Although quantitative information is lacking, it appears that D2-D3 deformations

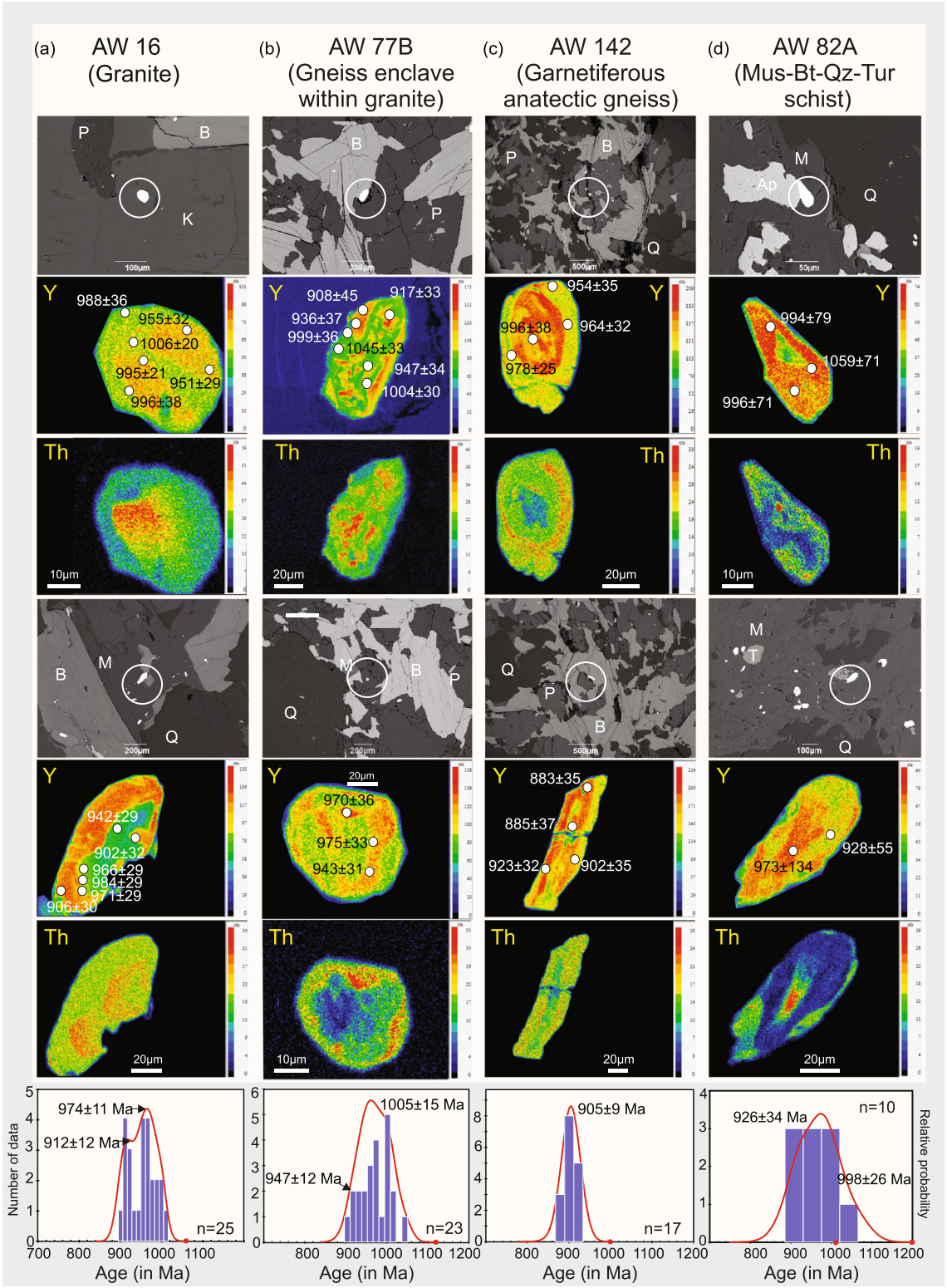

FIGURE 12: Monazite characteristics arranged column wise. Back scattered electron images of textural settings of monazites, representative Th and Y element maps of two monazites/per sample with embedded spot dates (±2σ) in Ma, and probability-density plots showing mean populations dates (in Ma) in monazites in four samples: (a) anatectic gneiss (AW 142), (b) anatectic gneiss enclave within granite (AW 77B), (c) steeply foliated granitoid (AW 16), and (d) mica schist (AW 82A). Acronyms used for minerals: plagioclase (P), K-feldspar (K), quartz (Q), muscovite/biotite (M/B), and apatite (A). Monazites are circled.

Table 3: Brief description of lithology, mineral assemblage, and summary of monazite textures, compositions, and chemical dates. Spot wise chemical composition, age, and 2σ error (in Ma) of monazites in Supplementary Material[3].

Sample number	Rock type and fabric relations	Textural setting of monazites	Zoning patterns and chemical variations in monazites	Number of analyzed grains and spots	Range of spot dates (±2σ) and mean dates (±2σ) in Ma
AW 142	Anatectic gneiss (Grt-Bt-Sil-Crd-Pl-Qtz) with penetrative pre-D2 and D2 composite fabrics that exhibit D3 upright folds. S3 fabric poorly developed.	Shot to long prismatic grains of 20-150 μm (long axis) occur at recrystallized Qtz-Pl grain/phase boundaries in leucosome, as inclusions in Grt, and within and boundaries of Bt flakes defining S2 fabric in the melanocratic matrix	Patchy-nebulous. Rarely concentrically zoned. ThO_2 (3.35-8.29 wt%) UO_2 (0.34-1.40 wt%) PbO (0.17-0.51 wt%) Y_2O_3 (1.56-3.03 wt%)	4 grains/16 spots	881 ± 55 to 925 ± 38 Ma 905 ± 9 Ma (MSWD = 0.59)
AW 82A	Anatectic gneiss (Bt-Kfs-Pl-Qtz) preserved as enclave within post D2 to syn D3 granite; shallow-dipping D2 fabric (with open folds) occur at high angle to the steep-dipping D3 foliation in granite	Rounded to short prismatic grains, 20-50 μm (long axis) within shape preferred Bt in the melanosome defining S2 gneissic foliation. Within aggregates of recrystallized quartz and feldspar in leucosomes, monazite does not exhibit shape alignment, and the grains are mostly anhedral.	Patchy-nebulous zoning. ThO_2 (5.1-9.18 wt%) UO_2 (0.1-0.71 wt%) PbO (0.17-0.43 wt%) Y_2O_3 (1.05-2.36 wt%)	5 grains/23 spots	908 ± 45 to 1045 ± 33 Ma 947 ± 12 Ma (MSWD = 0.63) 1005 ± 15 Ma (MSWD = 2.1)
AW 16	Mica schist (Mus-Apt-Qtz tourmaline) exhibits prominent S3 crenulation schistosity; sigmoid D2 schistosity defined by Mus is intrafolial to penetrative D3 schistosity	Subrounded to wedge-shaped prismatic grains (long axis~ 10 μm) elliptical to prismatic grains occur exclusively within Bt defined S3 fabric; a few grains also occur within the Q-domains interlayered with the M-domains.	Patchy to concentric zoning ThO_2 (0.95-3.83 wt%) UO_2 (0.17-1.13 wt%) PbO (0.08-0.27 wt%) Y_2O_3 (0.21-0.66 wt%)	5 grains/10 spots	908 ± 76 Ma to 1059 ± 71 Ma 972 ± 31 Ma (MSWD = 1.7)
AW 77B	Foliated granitoid (Qtz-Kfs-Pl-Bt, with retrograde Mus); coarse grained, inequigranular with well-developed steep-dipping D3 fabric defined by biotite flakes and quartz lentils wrapping around recrystallized K-feldspar porphyries	Ellipsoidal monazite grains (long axis 30-80 μm) occur within Bt, Kfs, and Qtz aggregates and exhibit no preferred alignment	Concentric-nebulous zoning. Rarely chemically homogenous ThO_2 (6.65-17.43 wt%) UO_2 (0.01-0.76 wt%) PbO (0.30-0.77 wt%) Y_2O_3 (0.29-2.04 wt%)	7 grains/25 spots	902 ± 32 Ma to 1006 ± 20 Ma 912 ± 12 Ma (MSWD = 0.27) 974 ± 11 Ma (MSWD = 2.1)

essentially involved a transition from thrust-dominated (D2) to wrench-dominated (D3) deformation that involved flipping of the *Y* and *Z* axes for orogen-parallel stretching caused by N-S shortening. The flipping of the *z*-axes from near-vertical during D2 to near-horizontal during D3 occurred irrespective of the nature of the rock types. But imbrications and linear trains of touching euhedral K-feldspar phenocrysts defining the steep-dipping W-trending magmatic fabrics in syn-D3 granitoids, subgrain chessboard microstructure in post-D2 granitoids ([28]; Figure 8(a)), and the pair of possibly conjugate near-vertical NNE and ENE melt-hosted D4 shear zones in the pink granitoids indicate that the D3-D4 deformations involving crustal shortening postdating D2 thrusting and crustal thickening were broadly contemporaneous with the emplacement of felsic melts. The transpressional W-striking D3 shears with moderately plunging stretching lineations and the near-vertical NNE and ENE shears indicate that the shortening direction was probably close to NNE-SSW. The expansive syn-D3 felsic plutonism is likely to have reduced the dynamic viscosity of the melt-bearing crust [73] and contributed to the nucleation of the D3 shear zones (cf. [74]). Also, the addition of large amounts of felsic magma during inhomogeneous progressive NNE-SSW shortening (cf. [75]) may have contributed to the flipping of the *Y*- and *z*-axes during D2-D3 for a similar orientation of orogen-parallel *x*-axis (Figures 10(a) and 10(b)).

5.2. Timing the Tectonic Events and Implications. Both monazite and zircon can be used to date high-T events, but monazites have the added advantage of being used to date low-T events [76–78] by fluid-induced dissolution-precipitation [78, 79] much below the temperature at which intracrystalline diffusion of Pb ceases in monazite and zircon, >750°C [80]. However, the problem with monazite dating is two-fold. First, chemical dates in monazites are associated with larger errors relative to isotopic dating. Second, chemical compositions of monazites are readily modified by fluid-induced processes [76–78], and therefore, there is less likelihood of preservation of older dates, unless the monazite grains are sequestered from fluid-aided alterations.

For the two samples dated with zircon, the Concordia dates are younger (ca. 1618 Ma) than the upper intercept age (1672 Ma). Given the large ellipses of the concordant points, it is possible that some of the points were actually affected by the lead loss and thus drive the Concordia dates towards younger age. Therefore, the upper intercept dates are considered to be more representative of the zircon age, although not very different than the Concordia dates. The U-Pb age of 1672 ± 18 Ma in the anatectic gneiss AW-22 (Figure 11(b)) pertains to the age of the pre-D2 high-grade metamorphism in the rocks and overlaps with the age of zircon cores in the foliated granite AW-5 (Figure 11(d)). The cores of these zircon grains are inherited and the date 926 ± 11 (±37) Ma (MSWD: 0.09; Figure 11(d)) obtained from a single zircon grain and the lower intercept date 921 ± 43 (±55) Ma (Figure 11(d)) obtained from the Discordia defined by 23 analyses at the rims of the zircon grains dates magmatic crystallization. This age is comparable with the existing Rb-Sr isochron dates for the Godhra granite, e.g., 965 ± 40 Ma [25], 955 ± 20 Ma [22], and 955 Ma [26]. The range of monazite ages (905 ± 35 Ma to 1059 ± 71 Ma) obtained from 74 spots in the four samples, including the Champaner white mica schist, straddle the Early Neoproterozoic U-Pb dates obtained in zircon (this study), and the existing Rb-Sr ages in the Godhra granite. These data suggest that the 1.0–0.9 Ga (mean value 0.95 Ga) corresponds to the intense D2-D3 deformation-metamorphism events and expansive emplacements of post-D2 to syn-D3 felsic intrusives. The granite AW-5 is likely to have formed due to partial melting of the Late Paleoproterozoic basement gneisses prior to experiencing the D2-D3 Early Neoproterozoic tectonism related to N-S crustal shortening induced by oblique accretion.

It is important to note that the Late Paleoproterozoic dates are not recorded in the cores of the analyzed monazite grains in the gneisses. It is likely that the older monazites, if present, were chemically modified due to dissolution-precipitation processes during the pervasive D2-D3 deformation-metamorphism experienced by all lithodemic units in the Godhra-Chhota Udepur sector.

5.3. Structural Evolution in the CGC-SMB vis-à-vis GC Sector. The lithological ensemble in the Chottanagpur Gneiss Complex (CGC) and the central and southern domains of the Satpura Mobile Belt (SMB) in the southern arm of the GIPFOB, also labeled as the Central Indian Tectonic Zone [18], is broadly similar ([19]; Figure 1(b)). Both in the CGC ([47, 81, 82] and references therein) and in the central and the southern domains of SMB [83–86], the basement is dominated by anatectic high-grade quartzo-feldspathic gneisses, garnet-sillimanite-K-feldspar bearing metapelites (khondalites), and charnockite-enderbite gneisses. These are intruded by granitoids that are massive, gneissose, foliated, or mylonitic. Nonanatectic amphibolite facies supracrustal rocks such as muscovite-biotite schist (±garnet ± sillimanite ± staurolite), micaceous quartzites, metadolomite/marble and meta-marl, and meta-arenaceous rocks constitute the third lithodemic component. Monazite chemical dates and Pb-Pb zircon dates in the lithodemic units in the CGC-SMB are compared by Banerjee et al. [19]. The dates in the CGC-SMB, disregarding those obtained from detrital zircon, are Late Paleoproterozoic/Early Mesoproterozoic (1.65–1.50 Ga) to Early Neoproterozoic (1.0 – 0.9 Ga); the oldest dates correspond with high-grade metamorphism in the anatectic gneisses and gneissose granitoids [85–91]. The supracrustal rocks and the younger granitoids are dominantly Early Neoproterozoic ([19], and references therein). The mid-Mesoproterozoic granitoids (1.45– 1.35 Ga), prolific in northern and central CGC [47], are not recorded in the central and southern segments of the SMB.

The Precambrian crystalline rocks of the CGC are traversed by a network of E/ENE-striking regional-scale steeply-dipping basement-piercing dominantly left-lateral transpressional shear zones [46, 47, 92–94]. The shear zones are commonly characterized by gently plunging stretching lineations, although steep stretching lineations are documented

in the centrally located parts of the CGC [46, 94], and along the orogen margins [92–94]. The flipped lineations in the Hundru Falls shear zone are attributed to perturbations in the convergence direction as a result of oblique NIB-SIB accretion [94]. The shear zones truncate a shallow-dipping carapace of allochthonous supracrustal rocks, Early Neoproterozoic (1.0 – 0.9 Ga) and Mid-Mesoproterozoic (1.45 – 1.35Ga; [47]) granitoid mylonites, and recumbently folded Late Paleoproterozoic/Early Mesoproterozoic (1.65–1.5 Ga) basement gneisses [19, 46, 47, 92, 94]. The thrusting of the allochthonous supracrustal rocks (formation of the shallow-dipping carapace) and the nucleation of E/ENE-striking transpressional steep shear zones are correlated with continued crustal shortening induced by Early Neoproterozoic SIB-NIB convergence [46, 47, 94].

The central and southern domains of the E-striking Satpura Mobile Belt (SMB) [95–97] exhibit significant structural similarities with those in the CGC. The recumbent folds in anatectic gneisses in these domains are attributed to southward thrusting leading to the interleaving of the basement rocks and the supracrustal rocks [96]. In the CGC, the thrusting is inferred to have been caused by northward translation of the allochthonous unit over the high-grade gneiss-granitoid basement [46, 47, 92–94]. Additionally, in these domains, the hinges of gently-plunging/subhorizontal E/W-closing folds in supracrustal rocks and anatectic gneisses with steep-diping axial surfaces [97, 98] are collinear with gently-plunging stretching lineations in the networks of steeply-inclined E-striking left-lateral transpressional shear zones [96]; some of these SMB shear zones exhibit steeply-plunging stretching lineations [96]. These shear zone networks originated due to oblique accretion between the Bundelkhand Craton in the north and the Bastar Craton in the south [85, 96, 98]; the variations in the orientations of the stretching lineations in the SMB are attributed to deformation strain partitioning [96].

Summarizing, it appears that the formation of shallow-dipping carapace and the nucleation of steep-dipping shears that affected the granite body, still hot and locally melt-bearing, was also Early Neoproterozoic in age. We suggest, therefore, that the Godhra-Chhota Udepur sector forms the westernmost extension of the E-striking arm of the GIPFOB or the CITZ that possesses a coherent Early Neoproterozoic accretion tectonic history involving oblique convergence between the NIB and the SIB.

5.4. The Southern Arm vis-à-vis the Western Arm (ADFB). The N/NNE-striking ADFB essentially comprises Archean basement gneisses and granitoids (BGC-I), some of which are deemed to be remobilized (Sandmata Mangalwar Complex, BGC-II) and are overlain by two sedimentary successions, namely, the Aravalli and Delhi Supergroup of rocks juxtaposed along multiple thrusts and shear zones [99–105; https://bhukosh.gsi.gov.in)]. The E-striking Early Neoproterozoic structures in the Godhra-Chhota Udepur sector at the southern tip of the ADFB (Figures 1(a) and 1(b)) are nearly orthogonal to the trend of the N/NNE-striking mesoscale structures in the ADFB (Figure 2); in fact, the ADFB structures are reoriented and terminated against the E-striking regional structures along the southern arm of the GIPFOB. Several features in the northern arm of the GIPFOB—especially the mesoscale structures and the chronology of magmato-metamorphic events [99–118]—differ considerably from those in the southern arm. First, the tectonic trends in the ADFB are dominantly NNE striking (Figure 2). At the southern end of the ADFB, the structural trends swing to an E-W orientation [27] (Figure 2). Second, the basement rocks of the ADFB are Mesoarchaean (~3.2 Ga; [99, 101, 112, 119–122]); these Mesoarchean amphibolite-facies tonalite-trondhjemite gneisses are intruded by Late Neoarchean (~2.5 Ga) granitoids at Berach, Untala, Gingla, and Ahar River [33, 100, 112, 121, 123–125]. By contrast, the basement rocks in the SMB-CGC and the GC sector (this study) are significantly younger, i.e., Late Paleoproterozoic to Early Mesoproterozoic [19]. Third, the basement (anatectic) gneisses [102, 103, 105, 106, 125–127] or remobilized BGC [128], associated granites (BGC-II), and the Sandmata granulites along the Kaliguman thrust are Paleoproterozoic in age (1.85–1.70 Ga; [103, 104, 106, 129, 130]). Fourth, the supracrustal rocks in South Aravalli share an angular unconformity with the basement gneisses [131, 132]. By contrast, an erosional contact between the basement rocks and the supracrustal rocks is lacking in the CGC. In the SMB, the unconformity suggested at Mansar [133–136] has been refuted [137, 138]. In the Godhra-Chhota Udepur sector, an erosional unconformity between the supracrustal rocks of low metamorphic grade and the basement gneisses/granitoids has been suggested [139], but no clear cut persistent unconformity/basal conglomerate layer at the intensely sheared contact between the two units was observed in this study, and we suggest the contact is tectonic in nature. Fifth, unlike in the southern arm of the GIPFOB, expansive Early Neoproterozoic shallow-dipping tectonic foliations are not reported in the ADFB. Open recumbent folds in Salumbar in southern parts of the ADFB [128] are locally developed and do not constitute a major fabric-forming event, as recorded in CGC-SMB. And finally, the regional D3 and D4 structures in the Aravalli and Delhi Supergroups in ADFB are identical [128], where the D4 upright thrust-related conjugate folds [128] are NNE and W-trending, with moderate to steep-plunging hinge lines. By contrast, the D4 structures in the Godhra-Chhota Udepur sector are E/WNW striking, near-orthogonal to the NNE-trending D4 folds [128] in ADFB.

6. Conclusions

Based on the foregoing discussion and the findings from this study and existing data, we suggest the curved nature of the N/NNE-trending structures at the southern tip of the ADFB (Figure 2) is due to the termination of the N/NNE-striking structures against the Early Neoproterozoic E-W-striking D2-D3 accretion-related deformation fabrics in the Godhra-Chhota Udepur sector that forms the westernmost extent of the E-striking southern arm of the GIPFOB. In other words, the Great Indian Proterozoic Fold Belt is composed of two distinct accretion orogens, e.g., the N/NNE-striking western arm formed due to the convergence

between the Marwar Craton (MC) in the west with the NIB, and the E-striking southern arm that resulted from the oblique accretion between the NIB and the SIB. We suggest that both, the MC-ADFB and NIB-SIB accretions, occurred during the Early Neoproterozoic, but the NIB-SIB accretion in the southern arm postdated the ADFB accretion orogen.

Data Availability

All data is included in table format and in figure (structural data) within the manuscript and in supplementary files submitted with the manuscript.

Additional Points

Highlights. (1) The Central Indian Tectonic Zone (CITZ) extends west till Godhra-Chhota Udepur (GC) [85]. (2) At GC Grenvillian-age N-S shortening led to thrust and wrench-dominated deformations [85]. (3) NNE-striking Aravalli Delhi Fold Belt (ADFB) juxtaposed against E-striking CITZ [82]. (4) The deformation structures in GC resulted from termination of ADFB against CITZ [80]. (5) Two accretion orogens ADFB and CITZ comprise Great Indian Proterozoic Fold Belt [83].

Conflicts of Interest

The authors declare that they have no conflicts of interest.

Acknowledgments

Anwesa Banerjee acknowledges the Research Fellowship awarded by the Indian Institute of Technology, Kharagpur (India) for carrying out this work. The work forms a part of her doctoral dissertation. NS acknowledges Goa University (India) for consenting to the collaborative research work. PN is thankful to the EPMA National Facility funded by Science and Engineering Research Board, Government of India (IRPHA grant no. IR/S4/ESF-16/2009 and CRG grant no. CRG/2019/000812) at the Department of Earth Sciences (IIT Bombay). We greatly appreciate the insightful and incisive comments provided by several journal reviewers; their views greatly helped in improving the technical aspect and the styling of the manuscript. We thank the Editor of the special volume for inviting us to contribute to this issue. Editorial handling of the manuscript by the Journal Associate Editor is greatly appreciated.

Supplementary Materials

Supplementary 1. Supplementary Material 1: locations of field photographs. The circled number-alphabet composites correspond to the figure numbers of field photographs in this study.

Supplementary 2. Supplementary Material 2: compositions and $^{207}Pb/^{206}Pb$ dates with 2σ errors obtained in zircon standard GJ-1.

Supplementary 3. Supplementary Material 3: electron probe microanalytical data of monazites, spot ages with 2σ errors in Ma, and error % computed following Prabhakar [62].

References

[1] A. B. Weil and A. Sussman, "Classification of curved orogens based on the timing relationships between structural development and vertical-axis rotation," in *Orogenic Curvature: Integrating Paleomagnetic and Structural Analyses*, A. J. Sussman and A. B. Weil, Eds., pp. 1–17, Geological Society of America Special Paper, 2004.

[2] S. T. Johnston, A. B. Weil, and G. Gutierrez-Alonso, "Oroclines: thick and thin," *Geological Society of America Bulletin*, vol. 125, no. 5-6, pp. 643–663, 2013.

[3] R. J. Musgrave, "Oroclines in the Tasmanides," *Journal of Structural Geology*, vol. 80, pp. 72–98, 2015.

[4] A. Jiménez-Bonilla, A. Crespo-Blanc, J. C. Balanyá, I. Expósito, and M. Díaz-Azpiroz, "Analog models of fold-and-thrust wedges in progressive arcs: a comparison with the Gibraltar Arc external wedge," *Frontiers Earth Science*, vol. 8, 2020.

[5] S. Marshak, "Salients, recesses, arcs, oroclines, and syntaxes; a review of ideas concerning the formation of map-view curves in fold-thrust belts," in *Thrust Tectonics and Hydrocarbon Systems*, K. R. McClay, Ed., vol. 82 of American Association of Petroleum Geologists Memoir, pp. 131–156, 2004.

[6] H. Hindle and M. Burkhard, "Strain, displacement and rotation associated with the formation of curvature on fold belts; the example of the Jura arc," *Journal of Structural Geology*, vol. 21, pp. 1089–1101, 1999.

[7] S. Eldredge, V. Bachtadse, and R. van der Voo, "Paleomagnetism and the orocline hypothesis," *Tectonophysics*, vol. 119, no. 1-4, pp. 153–179, 1985.

[8] A. B. Weil, A. Yonkee, and A. Sussman, "Reconstructing the kinematic evolution of curved mountain belts: internal strain patterns in the Wyoming Salient, Sevier thrust belt, U.S.A," *Geological Society of America Bulletin*, vol. 122, pp. 3–23, 2010.

[9] J. Macedo and S. Marshak, "Controls on the geometry of fold -thrust belt salient," *Geological Society of America Bulletin*, vol. 111, pp. 1808–1822, 1999.

[10] B. P. Radhakrishna and S. M. Naqvi, "Precambrian continental crust of India and its evolution," *Journal of Geology*, vol. 94, no. 2, pp. 145–166, 1986.

[11] C. Leelanandam, K. Burke, L. D. Ashwal, and S. J. Webb, "Proterozoic mountain building in Peninsular India: an analysis based primarily on alkaline rock distribution," *Geological Magazine*, vol. 143, pp. 195–212, 2006.

[12] N. Chatterjee, A. Bhattacharya, B. P. Duarah, and A. C. Mazumdar, "Late Cambrian reworking of Paleo-Mesoproterozoic granulites in Shillong-Meghalaya Gneissic Complex (Northeast India): evidence fromPTPseudosection analysis and monazite chronology and implications for East Gondwana assembly," *Journal of Geology*, vol. 119, no. 3, pp. 311–330, 2011.

[13] S. P. Mohanty, "Spatio-temporal evolution of the Satpura Mountain Belt of India: a comparison with the Capricorn Orogen of Western Australia and implication for evolution of the supercontinent Columbia," *Geoscience Frontiers*, vol. 3, no. 3, pp. 241–267, 2012.

[14] J. J. W. Rogers and M. Santosh, "Configuration of Columbia, a Mesoproterozoic supercontinent," *Gondwana Research*, vol. 5, no. 1, pp. 5–22, 2002.

[15] D. A. D. Evans and R. N. Mitchell, "Assembly and breakup of the core of Paleoproterozoic–Mesoproterozoic supercontinent," *Geology*, vol. 39, pp. 443–446, 2011.

[16] D. B. Yedekar, S. C. Jain, K. K. K. Nair, and K. K. Dutta, "The central Indian collision suture; Precambrian of Central India," *Geological Survey of India Special Publication*, vol. 28, pp. 1–27, 1990.

[17] Z. X. Li, S. V. Bogdanova, A. S. Collins et al., "Assembly, configuration, and break-up history of Rodinia: a synthesis," *Precambrian Research*, vol. 160, no. 1-2, pp. 179–210, 2008.

[18] B. P. Radhakrishna, "Suspect tectono-stratigraphic terrane elements in the Indian subcontinent," *Journal of the Geological Society of India*, vol. 34, pp. 1–24, 1989.

[19] A. Banerjee, N. Sequeira, and A. Bhattacharya, "Tectonics of the Greater India Proterozoic Fold Belt, with emphasis on the nature of curvature of the belt in west-central India," *Earth Science Reviews*, vol. 221, article 103758, 2021.

[20] P. Gupta, R. M. S. Fareeduddin, and K. Mukhopadhyay, "Stratigraphy and structure of Delhi Supergroup of rocks in central part of Aravalli range," *Records of the Geological Survey of India*, vol. 120, pp. 12–26, 1995.

[21] A. Sahni, S. K. Tandon, A. Jolly, S. Bajpai, A. Sood, and S. Srinivasan, "Upper Cretaceous dinosaur eggs and nesting sites from the Deccan-volcano sedimentary province of peninsular India," in *Dinosaur Eggs and Babies*, K. Carpenter, K. F. Hirsch, and J. R. Horner, Eds., pp. 204–226, Cambridge University Press, New York, NY, USA, 1994.

[22] K. Gopalan, J. R. Trivedi, S. S. Merh, P. P. Patel, and S. G. Patel, "Rb-Sr age of Godhra and related granites, Gujarat, India," *Earth and Planetary Science*, vol. 88, no. 1, pp. 7–17, 1979.

[23] N. Srimal and S. Das, "On the tectonic affinity of the Champaner Group of rocks, Eastern Gujarat," in *Abstract Volume, International Seminar on the Precambrian Crustal Evolution of Central and Eastern India*, pp. 226-227, UNESCO-lUGS-IGCP-368, Bhubaneswar, India, 1998.

[24] K. Shivkumar, P. B. Maithani, R. N. Parthasarathy, and K. K. Dwivedy, "Proterozoic rift in lower Champaners and its bearing in uranium mineralisation in Panchmahals district, Gujarat," *Annual Convention of Geological Society of India (Abstracts), [M.S. thesis]*, Department of Geology, University of Baroda, Vadodara, India, 1993.

[25] N. Goyal, P. C. Pant, P. K. Hansda, and B. K. Pandey, "Geochemistry and Rb-Sr age of the late Proterozoic Godhra granite of Central Gujarat, India," *Journal of the Geological Society of India*, vol. 58, pp. 391–398, 2001.

[26] A. R. Crawford, "The Precambrian geochronology of Rajasthan and Bundelkhand, northern India," *Canadian Journal of Earth Science*, vol. 7, no. 1, pp. 91–110, 1970.

[27] M. A. Mamtani, B. Karmakar, and S. S. Merh, "Evidence of polyphase deformation in gneissic rocks around Devgadh Bariya: implications for evolution of Godhra granite in the southern Aravalli region (India)," *Gondwana Research*, vol. 5, no. 2, pp. 401–408, 2002.

[28] M. A. Mamtani and R. O. Greiling, "Granite emplacement and its relation with regional deformation in the Aravalli Mountain Belt (India)–inferences from magnetic fabric," *Journal of Structural Geology*, vol. 27, no. 11, pp. 2008–2029, 2005.

[29] A. U. Joshi, "Fold interference patterns in Meso-Proterozoic Champaner fold belt (CFB) Gujarat, western India," *Journal of Earth System Science*, vol. 128, no. 3, p. 48, 2019.

[30] A. U. Joshi and M. A. Limaye, "Evidence of syndeformational granitoid emplacement within Champaner Group," *Journal of The Maharaja Sayajirao University of Baroda*, vol. 49, pp. 45–54, 2014.

[31] C. Srikarni and S. Das, "Stratigraphy and sedimentation history of Champaner Group, Gujarat," *Journal of the Indian Association of Sedimentologists*, vol. 15, pp. 93–108, 1996.

[32] B. B. Jambusaria and S. S. Merh, "Deformed greywacke conglomerates of Jaban near Shivrajpur, Panchmahals district, Gujarat," *Indian Minerals*, vol. 8, pp. 6–10, 1967.

[33] S. Das, *Deformation and Metamorphic History of the Precambrian Rocks in Northeastern Part of Vadodara District Gujarat with a Reference to the Stratigraphy and Tectonics, [Ph.D. thesis]*, University of Baroda, Vadodara, India, 2003.

[34] K. B. Joshi, J. Bhattacharjee, G. Rai et al., "The diversification of granitoids and plate tectonic implications at the Archaean–Proterozoic boundary in the Bundelkhand Craton, Central India," *Geological Society of London Special Publication*, vol. 449, no. 1, pp. 123–157, 2017.

[35] A. U. Joshi and M. A. Limaye, "Rootless calc-silicate folds in granite: an implication towards syn- to post-plutonic emplacement," *Journal of Earth System Science*, vol. 127, no. 5, p. 67, 2018.

[36] S. Das, P. K. Singh, and C. Sikarni, "A preliminary study of thermal metamorphism in the Champaner Group of rocks in Panchmahals and Vadodara districts of Gujarat," *Indian Journal of Geoscience*, vol. 63, pp. 373–382, 2009.

[37] M. A. Mamtani, R. O. Greiling, R. V. Karanth, and S. S. Merh, "Orogenic deformation and its relation with AMS fabric–an example from the southern Aravalli mountain belt, India," in *The Indian Subcontinent and Gondwana: A Palaeomagnetic and Rock Magnetic Perspective*, T. Radhakrishna and J. D. Piper, Eds., pp. 9–24, Memoir of the Geological Society of India, 1999.

[38] M. A. Mamtani, S. S. Merh, R. V. Karanth, and R. O. Greiling, "Time relationship between metamorphism and deformation in proterozoic rocks of the Lunavada region, Southern Aravalli Mountain Belt (India) – a microstructural study," *Journal of Asian Earth Science*, vol. 19, no. 1-2, pp. 195–205, 2001.

[39] K. Sen and M. A. Mamtani, "Magnetic fabric, shape preferred orientation and regional strain in granitic rocks," *Journal of Structural Geology*, vol. 28, no. 10, pp. 1870–1882, 2006.

[40] A. Nicolas and B. Ildefonse, "Flow mechanism and viscosity in basaltic magma chambers," *Geophysical Research Letters*, vol. 23, no. 16, pp. 2013–2016, 1996.

[41] J. H. Kruhl, "Prism- and basal-plane parallel subgrain boundaries in quartz: a microstructural geothermobarometer," *Journal of Metamorphic Geology*, vol. 14, no. 5, pp. 581–589, 1996.

[42] E. Fazio, P. Fiannacca, D. Russo, and R. Cirrincione, "Submagmatic to solid-state deformation microstructures recorded in cooling granitoids during exhumation of Late-Variscan crust in North-Eastern Sicily," *Geosciences*, vol. 10, no. 8, p. 311, 2020.

[43] S. Bhadra, S. Das, and A. Bhattacharya, "Shear zone-hosted migmatites (eastern India): the role of dynamic melting in the generation of REE-depleted felsic melts, and implications for disequilibrium melting," *Journal of Petrology*, vol. 48, no. 3, pp. 435–457, 2007.

[44] G. S. Solar and M. Brown, "Petrogenesis of migmatites in Maine, USA: possible source of peraluminous leucogranite

in plutons," *Journal of Petrology*, vol. 42, no. 4, pp. 789–823, 2001.

[45] J. Barraud, V. Gardien, P. Allemand, and P. Grandjean, "Analogue models of melt-flow networks in folding migmatites," *Journal of Structural Geology*, vol. 26, no. 2, pp. 307–324, 2004.

[46] N. Sequeira, S. Mahato, J. Rahl, S. Sarkar, and A. Bhattacharya, "The anatomy and origin of a syn-convergent Grenvillian-age metamorphic core complex, Chottanagpur Gneiss complex, Eastern India," *Lithosphere*, vol. 2020, no. 1, 2020.

[47] N. Sequeira, A. Bhattacharya, and E. Bell, "The ~1.4 Ga A-type granitoids in the "Chottanagpur crustal block" (India), and its relocation from Columbia to Rodinia?," *Geoscience Frontiers*, vol. 2021, 2021.

[48] M. A. P. C. Wiedenbeck, P. Alle, F. Corfu et al., "Three natural zircon standards for U-Th-Pb, Lu-Hf, trace element and REE analyses," *Geostandards Newsletter*, vol. 19, pp. 1–23, 1995.

[49] S. E. Jackson, N. J. Pearson, W. L. Griffin, and E. A. Belousova, "The application of laser ablation-inductively coupled plasma-mass spectrometry to in situ U-Pb zircon geochronology," *Chemical Geology*, vol. 211, no. 1-2, pp. 47–69, 2004.

[50] C. Paton, J. Hellstrom, B. Paul, J. Woodhead, and J. Hergt, "Iolite: freeware for the visualisation and processing of mass spectrometric data," *Journal of Analytical Atomic Spectrometry*, vol. 26, no. 12, pp. 2508–2518, 2011.

[51] M. S. Horstwood, J. Košler, G. Gehrels et al., "Community-derived standards for LA-ICP-MS U-(Th-)Pb geochronology – uncertainty propagation, age interpretation and data reporting," *Geostandards and Geoanalytical Research*, vol. 40, pp. 311–332, 2016.

[52] J. S. Stacey and J. D. Kramers, "Approximation of terrestrial lead isotope evolution by a two-stage model," *Earth and Planetary Science Letters*, vol. 26, no. 2, pp. 207–221, 1975.

[53] P. Vermeesch, "IsoplotR: a free and open toolbox for geochronology," *Geoscience Frontiers*, vol. 9, no. 5, pp. 1479–1493, 2018.

[54] J. M. Montel, S. Foret, M. Veschambre, C. Nicollet, and A. Provost, "Electron microprobe dating of monazite," *Chemical Geology*, vol. 131, no. 1-4, pp. 37–53, 1996.

[55] T. Deshmukh, N. Prabhakar, A. Bhattacharya, and K. Madhavan, "Late Paleoproterozoic clockwise *P-T* history in the Mahakoshal Belt, Central Indian Tectonic Zone: Implications for Columbia supercontinent assembly," *Precambrian Research*, vol. 298, pp. 56–78, 2017.

[56] F. S. Spear, J. M. Pyle, and D. Cherniak, "Limitations of chemical dating of monazite," *Chemical Geology*, vol. 266, no. 3-4, pp. 218–230, 2009.

[57] M. J. Jercinovic and M. L. Williams, "Analytical perils (and progress) in electron microprobe trace element analysis applied to geochronology: back-ground acquisition, interferences, and beam irradiation effects," *American Mineralogist*, vol. 90, no. 4, pp. 526–546, 2005.

[58] M. L. Williams, M. J. Jercinovic, P. Goncalves, and K. Mahan, "Format and philosophy for collecting, compiling, and reporting microprobe monazite ages," *Chemical Geology*, vol. 225, no. 1-2, pp. 1–15, 2006.

[59] N. Prabhakar and A. Bhattacharya, "Paleoarchean partial convective overturn in the Singhbhum Craton, Eastern India," *Precambrian Research*, vol. 231, pp. 106–121, 2013.

[60] K. R. Ludwig, "Isoplot/ex version 4.15, a geochronological toolkit for Microsoft Excel," *Berkeley Geochronology Center Special Publication*, vol. 4, p. 78, 2012.

[61] M. Knöper, R. Armstrong, M. Andreoli, and L. Ashwal, "The Steenkampskraal monazite vein: a subhorizontal stretching shear zone indicating extensional collapse of Namaqualand at 1033 Ma?," *Journal of African Earth Sciences*, vol. 31, pp. 38–38, 2000.

[62] N. Prabhakar, "Resolving poly-metamorphic Paleoarchean ages by chemical dating of monazites using multi-spectrometer U, Th and Pb analyses and sub-counting methodology," *Chemical Geology*, vol. 347, pp. 255–270, 2013.

[63] T. H. Bell and R. L. Hammond, "On the internal geometry of mylonite zones," *Journal of Geology*, vol. 92, no. 6, pp. 667–686, 1984.

[64] J.-P. Burg, P. Bale, and J. Girardeau, "Stretching lineation and transport direction in the Ibero-Armorican arc during the Siluro-Devonian collision," *Geodynamica Acta*, vol. 1, no. 1, pp. 71–87, 1987.

[65] H. Fossen, "Linear fabrics in Bergsdalen nappes, Southwest Norway: implications for deformational history and fold development," *Norsk Geologisk Tidsskrift*, vol. 73, pp. 95–108, 1993.

[66] H. Fossen, B. Tikoff, and C. T. Teyssier, "Strain modeling of transpressional and transtensional deformation," *Norsk Geologisk Tidsskrift*, vol. 74, pp. 134–145, 1994.

[67] B. Tikoff and D. Greene, "Stretching lineations in transpressional shear zones: an example from the Sierra Nevada Batholith, California," *Journal of Structural Geology*, vol. 19, no. 1, pp. 29–39, 1997.

[68] H. Fossen and B. Tikoff, "Extended models for transpression and transtension, and applications to tectonic settings," in *Continental Transpressional and Transtensional Tectonics*, R. E. Holdsworth, R. A. Strachan, and J. F. Dewey, Eds., pp. 15–33, Geological Society of London Special Publication, 1998.

[69] G. D. Williams, "Rotation of contemporary folds into the X direction during overthrust processes in Laksefjord, Finnmark," *Tectonophysics*, vol. 48, no. 1-2, pp. 29–40, 1978.

[70] G. I. Alsop, "Progressive deformation and the rotation of contemporary fold axes in the Ballybofey Nappe, Northwest Ireland," *Geological Journal*, vol. 27, no. 3, pp. 271–283, 1992.

[71] H. Fossen, *Structural Geology*, Camridge University Press, 2010.

[72] H. Fossen, C. Teyssier, and D. Whitney, "Transtensional folding," *Journal of Structural Geology*, vol. 56, pp. 89–102, 2013.

[73] J. L. Vigneresse and B. Tikoff, "Strain partitioning during partial melting and crystallizing felsic magmas," *Tectonophysics*, vol. 312, no. 2-4, pp. 117–132, 1999.

[74] A. Tommasi, A. Vauchez, L. A. Fernandes, and C. C. Porcher, "Magma-assisted strain localization in an orogen-parallel," *Tectonics*, vol. 13, pp. 421–437, 1994.

[75] R. McCaffrey, "Oblique plate convergence, slip vectors, and forearc deformation," *Journal of Geophysical Research*, vol. 97, pp. 8905–8915, 1992.

[76] F. Poitrasson, S. Chenery, and T. J. Shephard, "Electron microprobe and LA-ICP-MS study of monazite hydrothermal alteration:: Implications for U-Th-Pb geochronology and nuclear ceramics," *Geochimica et Cosmochimica Acta*, vol. 64, no. 19, pp. 3283–3297, 2000.

[77] S. Rekha, A. Bhattacharya, and T. A. Viswanath, "Microporosity linked fluid focusing and monazite instability in greenschist facies para-conglomerates, western India," *Geochimica et Cosmochimica Acta*, vol. 105, pp. 187–205, 2013.

[78] B. Rasmussen and J. R. Muhling, "Monazite begets monazite: evidence for dissolution of detrital monazite and reprecipitation of syntectonic monazite during low-grade regional metamorphism," *Contribution to Mineralogy and Petrology*, vol. 154, no. 6, pp. 675–689, 2007.

[79] B. Rasmussen, I. R. Fletcher, and N. J. McNaughton, "Dating low-grade metamorphic events by SHRIMP U-Pb analysis of monazite in shales," *Geology*, vol. 29, no. 10, pp. 963–966, 2001.

[80] E. Gardes, O. Jaoul, J. M. Montel, A. M. Seydoux-Guillaume, and R. Wirth, "Pb diffusion in monazite: An experimental study of Pb2++Th4+⇔2Nd3+ interdiffusion," *Geochimica et Cosmochimica Acta*, vol. 70, no. 9, pp. 2325–2336, 2006.

[81] T. M. Mahadevan, *Geology of Bihar and Jharkhand*, Geological Society of India, Bangalore, India, 2002.

[82] S. K. Acharyya, "A plate tectonic model for Proterozoic crustal evolution of Central Indian Tectonic Zone," *Gondwana Geological Magazine*, vol. 7, pp. 9–31, 2003.

[83] A. Roy and M. H. Prasad, "Tectonomagmatic history of tan shear zone and its environs, a preliminary study," *Geological Survey of India Special Publication*, vol. 64, pp. 273–287, 2001.

[84] A. Roy and M. H. Prasad, "Tectonothermal events in Central Indian Tectonic Zone (CITZ) and its implications in Rodinian crustal assembly," *Journal of Asian Earth Sciences*, vol. 22, pp. 115–129, 2003.

[85] S. K. Bhowmik, "The current status of orogenesis in the Central Indian Tectonic Zone: a view from its southern margin," *Geological Journal*, vol. 54, no. 5, pp. 2912–2934, 2019.

[86] A. Chattopadhyay, "Proterozoic orogenesis and crustal evolution in the Central Indian Tectonic Zone: current understanding from recent works," *Proceedings Indian National Science Academy*, vol. 86, pp. 99–106, 2020.

[87] A. Bhandari, N. Chandra Pant, S. K. Bhowmik, and S. Goswami, "~1.6 Ga ultrahigh-temperature granulite metamorphism in the Central Indian Tectonic Zone: insights from metamorphic reaction history, geothermobarometry and monazite chemical ages," *Geological Journal*, vol. 46, no. 2-3, pp. 198–216, 2011.

[88] A. Chattopadhyay, K. Das, Y. Hayasaka, and A. Sarkar, "Syn- and post-tectonic granite plutonism in the Sausar Fold Belt, central India: Age constraints and tectonic implications," *Journal of Asian Earth Sciences*, vol. 107, pp. 110–121, 2015.

[89] A. Chattopadhyay, A. Chatterjee, K. Das, and A. Sarkar, "Neoproterozoic transpression and granite magmatism in the Gavilgarh-tan shear zone, Central India: tectonic significance of U-Pb zircon and U-Th-total Pb monazite ages," *Journal of Asian Earth Sciences*, vol. 147, pp. 485–501, 2017.

[90] S. K. Bhowmik, S. A. Wilde, and A. Bhandari, "Zircon U-Pb/Lu-Hf and monazite chemical dating of the Tirodi biotite gneiss: implication for latest Palaeoproterozoic to early Mesoproterozoic orogenesis in the Central Indian Tectonic Zone," *Geological Journal*, vol. 46, no. 6, pp. 574–596, 2011.

[91] S. K. Bhowmik, S. A. Wilde, A. Bhandari, and A. Basu Sarbadhikari, "Zoned monazite and zircon as monitors for the thermal history of granulite terranes: an example from the Central Indian Tectonic Zone," *Journal of Petrology*, vol. 55, no. 3, pp. 585–621, 2014.

[92] N. Sequeira and A. Bhattacharya, "Early Neoproterozoic Accretion at the Northern Margin of the Chottanagpur Gneiss Complex, Eastern India," *Tectonics*, vol. 40, 2021.

[93] A. Bhattacharya, S. Rekha, N. Sequeira, and A. Chatterjee, "Transition from shallow to steep foliation in the early Neoproterozoic Gangpur accretionary orogen (Eastern India): mechanics, significance of mid-crustal deformation, and case for subduction polarity reversal?," *Lithos*, vol. 348-349, p. 105196, 2019.

[94] N. Sequeira and A. Bhattacharya, "Early Neoproterozoic deformation kinematics in the Chottanagpur gneiss complex (eastern India): evidence from the curvilinear Hundru falls shear ZoneAnalysis," *Lithosphere*, vol. 2020, no. 1, 2020.

[95] S. P. Mohanty, "Evolution of the "central Indian tectonic zone": a critique based on the study of the Sausar Belt," in *Structural Geometry of Mobile Belts of the Indian Subcontinent*, T. K. Biswal, S. K. Ray, and B. Grasemann, Eds., pp. 57–89, Springer, 2020.

[96] A. Chattopadhyay and L. Khasdeo, "Structural evolution of Gavilgarh-tan shear zone, Central India: a possible case of partitioned transpression during Mesoproterozoic oblique collision within Central Indian Tectonic Zone," *Precambrian Research*, vol. 186, no. 1-4, pp. 70–88, 2011.

[97] A. Chattopadhyay and D. Bhattacharjee, "Repeated reactivation of the Gavilgarh-tan shear zone, Central India: implications for the tectonic survival of deep-seated intracontinental fault zones," *Journal of Asian Earth Sciences*, vol. 186, p. 104051, 2019.

[98] A. Roy, H. M. Ramachandra, and B. K. Bandopadhyay, "Supracrustal belts and their significance in the crustal evolution of Central India," *Geological Survey of India Special Publication*, vol. 55, pp. 361–380, 2000.

[99] M. Wiedenbeck, J. N. Goswami, and A. B. Roy, "Stabilization of the Aravalli craton of northwestern India at 2.5 Ga: an ion microprobe zircon study," *Chemical Geology*, vol. 129, pp. 325–340, 1996.

[100] M. Wiedenbeck, J. N. Goswami, and A. B. Roy, "An ion microprobe study of single zircons from the Amet granite, Rajasthan," *Journal of the Geological Society of India*, vol. 48, pp. 127–137, 1996.

[101] M. Wiedenbeck and J. N. Goswami, "High precision 207Pb206Pb zircon geochronology using a small ion microprobe," *Geochimica et Cosmochimica Acta*, vol. 58, pp. 2135–2141, 1994.

[102] I. S. Buick, C. Allen, M. Pandit, D. Rubatto, and J. Hermann, "The Proterozoic magmatic and metamorphic history of the banded gneiss complex, Central Rajasthan, India: LA-ICP-MS U-Pb zircon constraints," *Precambrian Research*, vol. 151, pp. 119–142, 2006.

[103] I. S. Buick, C. Clark, D. Rubatto, J. Hermann, M. Pandit, and M. Hand, "Constraints on the Proterozoic evolution of the Aravalli–Delhi Orogenic belt (NW India) from monazite geochronology and mineral trace element geochemistry," *Lithos*, vol. 120, pp. 511–528, 2010.

[104] S. K. Bhowmik, H. J. Bernhardt, and S. Dasgupta, "Grenvillian age high-pressure upper amphibolite-granulite metamorphism in the Aravalli-Delhi Mobile Belt, northwestern India: new evidence from monazite chemical age and its implication," *Precambrian Research*, vol. 178, pp. 168–184, 2010.

[105] S. K. Bhowmik, S. Dasgupta, S. Baruah, and D. Kalita, "Thermal history of a late Mesoproterozoic paired metamorphic belt (?) during Rodinia assembly: new insight from medium-pressure granulites from the Aravalli-Delhi Mobile Belt, northwestern India," *Geoscience Frontiers*, vol. 9, pp. 335–354, 2018.

[106] A. Prakash, L. Saha, I. Petrik, M. Janak, and A. Bhattacharya, "Metamorphic evolution of Palaeoproterozoic anatectic migmatites in the eastern part of the Aravalli–Delhi Fold Belt, India: constraints from thermodynamic modelling and monazite dating," *Geological Magazine*, vol. 155, pp. 955–978, 2018.

[107] J. D'Souza, N. Prabhakar, Y. Xu, K. K. Sharma, and H. Sheth, "Mesoarchaean to Neoproterozoic (3.2-0.8 Ga) crustal growth and reworking in the Aravalli craton, northwestern India: Insights from the Pur-Banera supracrustal belt," *Precambrian Research*, vol. 332, article 105383, 2019.

[108] P. Kaur, A. Zeh, N. Chaudhri, A. Gerdes, and M. Okrusch, "Archaean to Palaeoproterozoic crustal evolution of the Aravalli mountain range, NW India, and its hinterland: the U–Pb and Hf isotope record of detrital zircon," *Precambrian Research*, vol. 187, pp. 155–164, 2011.

[109] P. Kaur, A. Zeh, and N. Chaudhri, "Archean crustal evolution of the Aravalli banded gneissic complex, NW India: constraints from zircon U-Pb ages, Lu-Hf isotope systematics, and whole-rock geochemistry of granitoids," *Precambrian Research*, vol. 327, pp. 81–102, 2019.

[110] S. M. Chatterjee, M. Roy Choudhury, S. Das, and A. Roy, "Significance and dynamics of the Neoproterozoic (810 Ma) Phulad shear zone, Rajasthan, NW India," *Tectonics*, vol. 36, pp. 1432–1454, 2017.

[111] S. M. Chatterjee, A. K. Sarkar, A. Roy, and A. Manna, "Mid-Neoproterozoic tectonics of northwestern India: evidence of stitching pluton along 810 Ma Phulad shear zone," *Tectonics*, vol. 39, 2020.

[112] A. B. Roy and A. Kröner, "Single zircon evaporation ages constraining the growth of the Archaean Aravalli craton, northwestern Indian shield," *Geological Magazine*, vol. 133, pp. 333–342, 1996.

[113] M. K. Pandit, L. M. Carter, L. D. Ashwal et al., "Age, petrogenesis and significance of 1 Ga granitoids and related rocks from the Sendra area, Aravalli craton, NW India," *Journal of Asian Earth Science*, vol. 22, pp. 363–381, 2003.

[114] C. Dharma Rao, M. Santosh, R. Purohit, J. Wang, X. Jiang, and T. Kusky, "LA-ICP-MS U–Pb zircon age constraints on the Paleoproterozoic and Neoarchean history of the Sandmata Complex in Rajasthan within the NW Indian Plate," *Journal of Asian Earth Sciences*, vol. 42, pp. 286–305, 2011.

[115] A. B. Roy, A. Kroner, P. K. Bhattachaya, and S. Rathore, "Metamorphic evolution and zircon geochronology of early Proterozoic granulites in the Aravalli Mountains of northwestern India," *Geological Magazine*, vol. 142, pp. 287–302, 2005.

[116] W. Wang, P. A. Cawood, M. K. Pandit, M. F. Zhou, and W. T. Chen, "Zircon U–Pb age and Hf isotope evidence for an Eoarchaean crustal remnant and episodic crustal reworking in response to supercontinent cycles in NW India," *Journal of the Geological Society of India*, vol. 174, pp. 759–772, 2017.

[117] W. Wang, P. Cawood, M. K. Pandit, and Z. Mei-Fu, *Evolving Passive and Active Margin Tectonics of the Paleoproterozoic Aravalli Basin*, Geological Society of America Bulletin, 2018.

[118] N. R. McKenzie, N. C. Hughes, P. M. Myrow, D. M. Banerjee, M. Deb, and N. J. Planavsky, "New age constraints for the Proterozoic Aravalli–Delhi successions of India and their implications," *Precambrian Research*, vol. 238, pp. 120–128, 2013.

[119] L. Saha, D. Frei, A. Gerdes et al., "Crustal geodynamics from the Archaean Bundelkhand Craton, India: constraints from zircon U–Pb–Hf isotope studies," *Geological Magazine*, vol. 153, pp. 179–192, 2016.

[120] M. E. A. Mondal, J. N. Goswami, M. P. Deomurari, and K. K. Sharma, "Ion microprobe $^{207}Pb/^{206}Pb$ ages of zircons from the Bundelkhand massif, northern India: implications for crustal evolution of the Bundelkhand–Aravalli protocontinent," *Precambrian Research*, vol. 117, pp. 85–100, 2002.

[121] A. K. Choudhary, K. Gopalan, and C. A. Sastry, "Present status of the geochronology of the Precambrian rocks of Rajasthan," *Tectonophysics*, vol. 105, pp. 131–140, 1984.

[122] K. Gopalan, J. D. Macdougall, A. B. Roy, and A. V. Murali, "Sm-Nd evidence for 3.3 Ga old rocks in Rajasthan, northwestern India," *Precambrian Research*, vol. 48, pp. 287–297, 1990.

[123] T. V. Sivaraman and A. L. Odom, "Zircon geochronology of Berach granite of Chittorgarh, Rajasthan," *Journal of the Geological Society of India*, vol. 23, pp. 575–577, 1982.

[124] C. A. Sastry, "Geochronology of the Precambrian rocks from Rajasthan and northeastern Gujarat," *Special Publication of the Geological Survey of India*, vol. 25, p. 96, 1992.

[125] D. B. Guha and R. S. Garkhal, "Early Proterozoic Aravalli metasediments and their relation with the Ahar River granite around Udaipur, Rajasthan," *Journal of the Geological Society of India*, vol. 42, pp. 327–335, 1993.

[126] A. B. Roy, "Evolution of the Precambrian crust of the Aravalli mountain range," in *Developments in Precambrian Geology*, A. B. Roy, Ed., pp. 327–347, Elsevier, 1990.

[127] L. Saha, S. K. Bhowmik, M. Fukuoka, and S. Dasgupta, "Contrasting episodes of regional granulite-facies metamorphism in enclaves and host gneisses from the Aravalli–Delhi mobile belt, NW India," *Journal of Petrology*, vol. 49, pp. 107–128, 2008.

[128] K. Naha and S. Mohanty, "Structural studies in the pre-Vindhyan rocks of Rajasthan: a summary of work of the last three decades," *Proceedings of the Indian Academy of Sciences (Earth Planetary Sciences)*, vol. 99, no. 2, pp. 279–290, 1990.

[129] S. K. Bhowmik and S. Dasgupta, "Tectonothermal evolution of the banded gneissic complex in Central Rajasthan, NW India: present status and correlation," *Journal Asian Earth Sciences*, vol. 49, pp. 339–348, 2012.

[130] A. B. Roy, A. Kröner, S. Rathore, V. Laul, and R. Purohit, "Tectono-metamorphic and geochronologic studies from Sandmata complex, northwest Indian shield: implications on exhumation of late-palaeoproterozoic granulites in an archaean-early palaeoproterozoic granite-gneiss terrane," *Journal of the Geological Society of India*, vol. 79, no. 4, pp. 323–334, 2012.

[131] A. M. Heron, *The Geology of Central Rajputana*, Memoirs of the Geological Society of India, 1953.

[132] K. Naha, D. K. Mukhopadhyay, R. Mohanty, S. K. Mitra, and T. K. Biswal, "Significance of contrast in the early stages of the structural history of the Delhi and the pre-Delhi rock groups

in the Proterozoic of Rajasthan, western India," *Tectonophysics*, vol. 105, no. 1-4, pp. 193–206, 1984.

[133] S. Mohanty, "Stratigraphic position of the Tirodi gneiss in the Precambrian terrane of Central India: evidence from the Mansar area, Nagpur district, Maharashtra," *Journal of the Geological Society of India*, vol. 42, pp. 55–55, 1993.

[134] A. K. Mohanty and S. Mohanty, "Structural patterns in the Sausar group around Mansar, Nagpur district, Maharashtra," *Journal of the Geological Society of India*, vol. 48, pp. 559–566, 1996.

[135] S. Mohanty, "Structural evolution of Sausar group around Parseoni, Nagpur district, Maharashtra: its implication for stratigraphy," *Journal of the Geological Society of India*, vol. 60, pp. 309–316, 2002.

[136] S. P. Mohanty, "Structural-stratigraphic relations in Precambrain rocks of Sausar Belt, Central India," *Gondwana Geological Magazine Special*, vol. 7, pp. 109–117, 2003.

[137] A. Chattopadhyay, A. K. Huin, and A. S. Khan, "Structural framework of Deolapar area, Central India and its implications for Proterozoic nappe tectonics," *Gondwana Research*, vol. 6, no. 1, pp. 107–117, 2003.

[138] A. Chattopadhyay, A. S. Khan, A. K. Huin, and B. K. Bandyopadhyay, "Reinterpretation of stratigraphy and structure of Sausar Group in Ramtek-Mansar-Kandri area, Maharashtra, Central India," *Journal of the Geological Society of India*, vol. 61, pp. 75–89, 2003.

[139] W. T. Blanford, "On the geology of Taptee and Nerbudda valleys and some adjoining districts," *Memoirs of the Geological Survey of India*, vol. 6, pp. 176–182, 1869.